

Programming the microstructure of magnetic nanocomposites in DLP 3D printing

*Original*

Programming the microstructure of magnetic nanocomposites in DLP 3D printing / Lantean, S.; Roppolo, I.; Sangermano, M.; Hayoun, M.; Dammak, H.; Rizza, G.. - In: ADDITIVE MANUFACTURING. - ISSN 2214-8604. - ELETTRONICO. - 47:(2021), p. 102343. [10.1016/j.addma.2021.102343]

*Availability:*

This version is available at: 11583/2933269 since: 2021-10-20T12:28:02Z

*Publisher:*

Elsevier B.V.

*Published*

DOI:10.1016/j.addma.2021.102343

*Terms of use:*

This article is made available under terms and conditions as specified in the corresponding bibliographic description in the repository

*Publisher copyright*

Elsevier postprint/Author's Accepted Manuscript

© 2021. This manuscript version is made available under the CC-BY-NC-ND 4.0 license  
<http://creativecommons.org/licenses/by-nc-nd/4.0/>. The final authenticated version is available online at:  
<http://dx.doi.org/10.1016/j.addma.2021.102343>

(Article begins on next page)

## Programming the microstructure of magnetic nanocomposites in DLP 3D printing

Simone Lantean<sup>1,2</sup>, Ignazio Roppolo<sup>1,3\*</sup>, Marco Sangermano<sup>1</sup>, Marc Hayoun<sup>2</sup>, Hichem Dammak<sup>2,4</sup>, Giancarlo Rizza<sup>2</sup>

1. Department of Applied Science and Technology, Politecnico di Torino, Duca degli Abruzzi, 24, 10124, Torino, Italy
2. Laboratoire des Solides Irradiés (LSI), Institut Polytechnique de Paris, CEA/DRF/IRAMIS, CNRS, Ecole polytechnique, Route de Saclay, 91128 Palaiseau, France
3. Center for Sustainable Future Technologies, Istituto Italiano di Tecnologia, Via Livorno 60, 10144, Torino, Italy
4. Laboratoire Structures Propriétés et Modélisation des Solides, CentraleSupélec, CNRS, Université Paris-Saclay, F 91190 Gif-sur-Yvette, France

E-mail: [ignazio.roppolo@polito.it](mailto:ignazio.roppolo@polito.it)

### Abstract

The ability to program the behavior of magneto-reactive polymers requires the fine control of their magnetic microstructure during each step of the printing process. Here, a systematic study of magnetically driven self-assembly of  $\text{Fe}_3\text{O}_4$  nanoparticles into chain-like structures is presented and used in a 3D printable formulation. The kinetics of chains formation, as well as their rotation, are studied by varying several experimental parameters: i.e. the viscosity of the formulation, the content of nanoparticles, the intensity of the applied magnetic field, and its application time. Experimental results are coupled to numerical simulations based on the dipolar approximation model, and the collected data are used to produce a dataset to precisely program the microstructure during the printing step. Thus, a desired microstructure in a 3D printed piece can be obtained by controlling the orientation and the length of the magnetic chains in each printed layer. This is achieved by modifying a commercial Digital Light Processing (DLP) 3D printer to apply magnetic fields of tunable intensity and direction. Finally, as a proof of concept, a pyramid-like structure was 3D printed, where each layer contains a specific and spatially oriented microstructure.

## 1. Introduction

Nowadays, polymeric 3D printing technology is widespread in several industrial fields, especially in those where customization and complex shapes are important added values for the products, such as automotive, fashion, design, and architecture [1,2]. However, its advantages are not only limited to design freedom or cost reduction [3–5] but can also be extended to its flexibility and adaptability to new materials. Indeed, in the last few years, increasing efforts were made to explore new fields of application in the synthesis of functional materials and the fabrication of printable composites [6–15]. Among them, a new field of research has recently emerged: the printing of smart materials capable of changing their shapes and properties under the effect of external stimuli, *i.e.* the so-called 4D printing, where time is the fourth dimension [16–20]. 4D printing is expected to bring breakthrough improvements in several domains, such as robotics, sensors, and biomedicine [21–23]. In polymeric 4D printing, smart materials, either neat polymers or composites, must possess one or more functions that can be activated by physicochemical stimuli including, solvents [24,25], light [26–28], temperature [29–33], electric charges [34–36], and pH [37,38]. Among these, the use of magnetic fields is of particular interest as they are harmless to the body, and their intensity and direction can be easily controlled in remote, without physical contact between the source and the object. [39,40]. However, as most of the polymers are not magnetic, this property must be implemented. The easiest strategy is to embed magnetic fillers within the polymeric host matrix. In particular, soft magneto-responsive composite polymers (MRCP) are ideal candidates for 4D applications, as they can be easily deformed by the use of low-intense fields [39-42].

The magnetic force ( $\mathbf{F}$ ) in a MRCP is directly proportional to the magnetic field gradient and the magnetization of the material, *i.e.*  $\mathbf{F} = \nabla(\mathbf{M} \cdot \mathbf{B})$ , where  $\mathbf{M}$  is the magnetic moment and  $\mathbf{B}$  the applied magnetic induction. Being  $\mathbf{M}$  linearly proportional to the amount of dispersed magnetic fillers, magnetic force can be controlled by the NPs loading [43,44]. However, high loads lead to a number of issues in the processing of the material, such as reduced material stability, poor dispersion of the fillers, bad adhesion within the printed layers, and poor mechanical properties. On the other hand, an alternative strategy to use the magnetic force without increasing the amount of the NPs has recently emerged, which consists in organizing the magnetic dipoles and/or the microstructure of the MRCPs. Indeed, when magnetic particles are dispersed within a liquid medium and exposed to a uniform magnetic field, their magnetic dipoles arrange in a head-to-tail configuration [45-47]. The magnetic forces produced in such systems lead to the spontaneous assembling of NPs in chain-like structures aligned along the

field vector [48-53]. The shape of the elongated aggregates creates a magnetic anisotropy characterized by a preferential magnetization direction, i.e. the easy axis of magnetization, along the major axis of the structure. This approach can be used in liquids as well as in polymer solutions, molten polymers or photocurable formulations. The solidification/curing of the polymer matrix freezes the self-assembled particles into a defined microstructure and fixes the magnetic anisotropy of the composite material. In these conditions, the application of an external magnetic field produces a magnetic torque, i.e.  $\mathbf{M} \times \mathbf{B}$  [54-57], which forces the chains to rotate and to align along the field direction. As they are embedded structures, the magnetic torque is then transferred to the host matrix. Thus, by controlling the arrangement of the magnetic chains it is possible to finely predict the mechanical transformation -motion, shape-shifting or rotation - of the 4D printed MRCPs [58,59].

In literature, the fabrication of 3D printed MRCPs has been reported for Direct Ink Writing (DIW) [60-63], Fused Filament Fabrication (FFF) [64-68], Stereolithography (SL) and Digital Light Processing (DLP) [69-73] technologies. For instance, Hu *et al* [74] demonstrated different types of motions both in dry and wet environments of magneto-driven robots. Lu *et al* [75] developed milli-robots with magneto-responsive micro-legs, mimicking the walking. Kim *et al* [76] developed a magnetically assisted Direct Ink Writing (DIW) 3D printer for the fabrication of magnetic soft composite films with programmable magnetic domains. Kim *et al* [59] developed a photo-lithography-based system where the direction of the external magnetic and the region of the resin to be irradiated are selectively chosen. The same approach was used to 3D print micron-size twist-type swimmer in a 2-photons polymerization process [77,78]. Martin *et al* [79] controlled the axial orientation of alumina platelets decorated with magnetic particles during the DLP printing process, leading to the fabrication of composite materials with biomimetic microstructures and enhanced impact resistance.

Although a rich literature exists on the self-assembly of magnetic particles [60-81], there is a lack of comprehensive and systematic investigation to use this process to 3D print of macroscopic magneto-reactive polymers. Thus, the aim of this work is to bridge this gap by investigating how the microstructure can be tuned and spatially controlled during the printing step to obtain an object having optimum programmable properties.

Digital Light Processing (DLP) has been selected as 3D printing technology, as it utilizes a photo-curable resins in a vat, wherein the magnetic fillers can be easily dispersed and undergo self-assembly process upon the application of an external magnetic field. Although FFF and DIW technologies offer these possibilities, eventually even with a higher content of magnetic nanoparticles, and consequent higher magnetic response [62, 65, 66], the simultaneous

formation of the microstructure in an entire layer can be realized only by DLP technology, together with other technological advantages [82,83]. This allows orienting the magnetic microstructure for each subsequent layer, and thus producing objects with spatially oriented magnetic anisotropies and programmable mechanical properties.

Here, the self-assembly process of magnetite nanoparticles ( $\text{Fe}_3\text{O}_4$  NPs) dispersed in a photocurable resin and exposed to an external field has been investigated *in situ* by optical microscopy. In particular, we investigated how the average length of the chains can be tuned by modifying the printing parameters (viscosity of the resin, amount of fillers, applied magnetic field,...) and we defined the optimum conditions for printing a composite object possessing a homogeneous microstructure. Then, we studied how the microstructure can be spatially oriented and we defined a stability landscape for the microstructure during the rotation process. Experimental results have been interpreted by using the dipolar approximation model and numerical simulations. We propose a simple and cheap modification easily implemented to all the existing *open source* DLP printers to apply controlled magnetic fields during the printing process and program the microstructures of the processed magneto composite polymers. Finally, as a proof of concept and using our previous knowledge on magneto-composite polymers processing by DLP [84], we 3D printed objects with programmed microstructures witnessing that the developed modification module is effective in controlling the dimension and the orientation of the magnetic chains in each printed layer of the object.

## **2. Results and Discussion**

### **2.1. Controlling the microstructure through the self-assembly of $\text{Fe}_3\text{O}_4$ nanoparticles**

In this work, formulations are obtained by loading Ebecryl 232 acrylic resin with 50-100 nm  $\text{Fe}_3\text{O}_4$  nanofillers, using butyl acrylate as reactive diluent, as reported in experimental section and based on previous studies reported in Ref. [84]. Here, we first study how to control both the average length and the rotation of the self-assembled chains in the X-Y plane. We then transpose the problem into the third spatial dimension, Z-axis, to control the orientation of the magnetic chains in the whole space. For the sake of clarity, and so as not to weigh down the text, in the following the kinetics of the self-assembling process is only reported for a single experimental set up in terms of applied magnetic field, viscosity, and filler concentration. This is a formulation containing 60 wt.% of Ebecryl (Eb) 232 acrylic resin and 40 wt.% of Butyl acrylate (BA) used as reactive diluent, noted as 60Eb40BA, in which 3 wt.% of  $\text{Fe}_3\text{O}_4$  particles

(50-100 nm) are dispersed. The viscosity of the system has been measured to be  $\eta = 0.05 = 0.05 \text{ Pa s}$  and the evolution of the microstructure has been followed after the application of magnetic field of 30 mT. This reference system has been labeled as 60Eb40BA\_3NP\_30mT. Results corresponding to other formulations are reported in supporting information (SI) file. Experimental results have been coupled to molecular dynamics simulation by minimizing the total energy of the system through the Evans and Beeler procedure [85,86]. Details of the simulation are reported in SI file.

Figure 1.a shows the time-frame evolution of the self-assembly process up to 110 minutes. The initial configuration ( $t = 0$ ) is characterized by the presence of randomly dispersed inhomogeneous island-like structures without preferential spatial orientation (see inset). Within few seconds after the application of the magnetic field ( $t = 1 \text{ min}$ ,  $\mathbf{B} = 30 \text{ mT}$ ), the dipolar interactions allow isolated NPs to aggregate and to efficiently form elongated structures, that can reach several micrometers in length. This behavior has been qualitatively reproduced in Figure 1.b by using numerical simulations where the energy minimization leads to the formation of filamentary structures growing along the direction of the applied field. Considering the chains as prolate ellipsoids, the average temporal evolution of their length,  $L$ , and width,  $W$ , is shown in Figure 1.c. Their length  $L$  (full black squares) is observed to rapidly increase within the first 10 minutes and then, for longer times, to slow down reaching an almost asymptotic plateau at about  $120 \mu\text{m}$ . Although the chains continue to elongate over time, this occurs at a much slower rate, see for instance Figure S3. Thus, for our purposes, the formation of the plateau is used to determine average length of the microstructure before to start the printing process. Conversely, the average width of the chains,  $W$ , (full red circles) remains nearly constant, at about  $27 \mu\text{m}$ , for the duration of the self-assembly process.

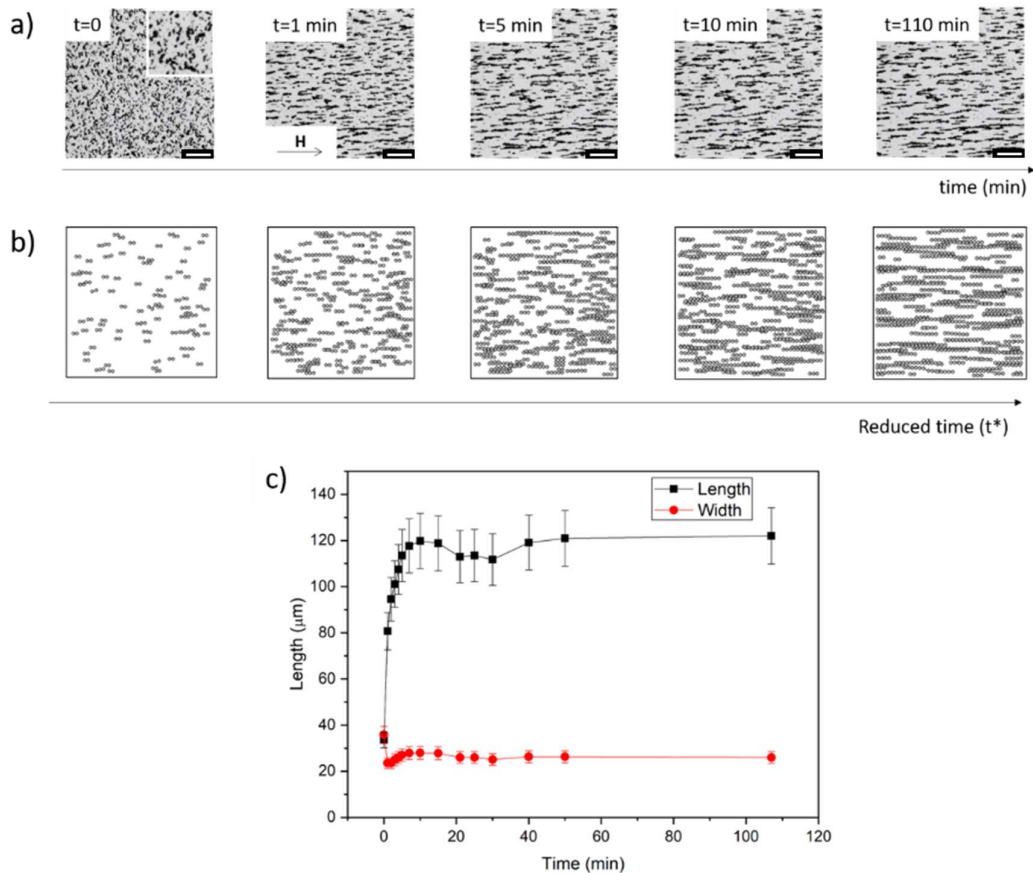


**Figure 1:** a) Experimental time evolution of the self-assembling process and the formation of the chains of nanoparticles aligned along the direction of the magnetic field (scale bar is  $500 \mu\text{m}$ ) b) time-frame numerical simulations of the chains (isolated NPs are absent), and c) experimental evolution of the length ( $L$ ) and the width ( $W$ ) of the chains of NPs. The reduced time is defined in section 1 of SI.

Insights into the chains' formation and elongation is obtained by reporting how the length distribution evolves as a function of time, Figure 2.a. The experimental data display a log-normal function with a peak associated to the shorter aggregates and a tail toward the longer chains. It is observed that the peak of the distribution decreases with time while the relative frequency of longer chains, the tail of the distribution, increases. At the same time, in the first few minutes after the application of the field the total number of the wire structures decreases dramatically reaching a plateau after about 5 minutes, Figure 2.b. These experimental trends are coherent with the existing literature [50,87]. As indicated by numerical simulations (Figure 2.c) the self-assembling involves the attraction of isolated NPs or smaller chains by the elongated structures, and their aggregation to a longer chain at its head or tail extremity, where

the interaction among the NPs is maximum. This mechanism can be thus associated to a coalescence-like process [88].

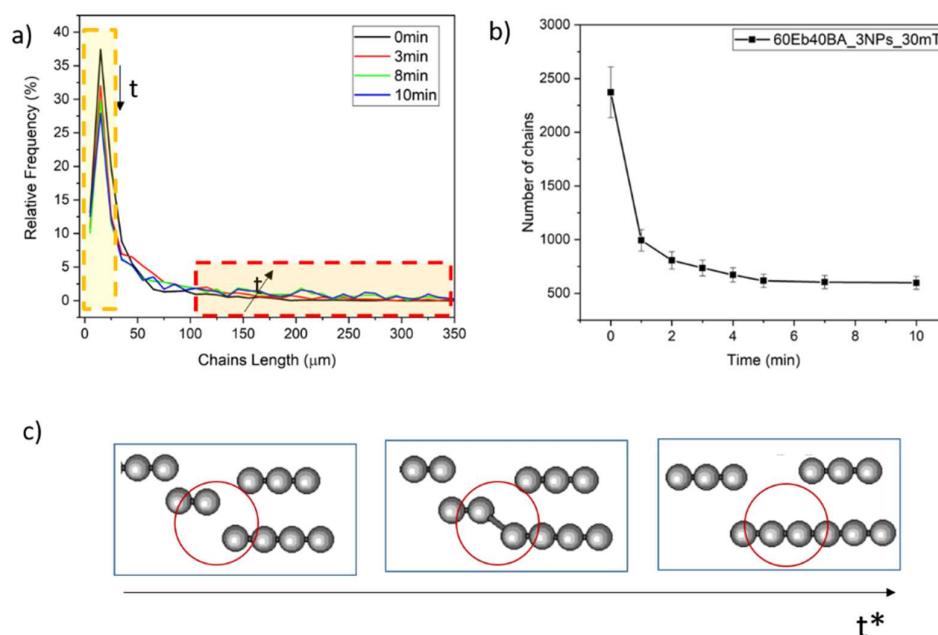


**Figure 2:** a) Time evolution of the distribution of the chains' lengths time up to 10 min, b) evolution of the number of aggregates, c) numerical simulations showing the growth of a chain by the aggregation at its end of a small NP aggregate.

In a second step, the effect of the magnetic field intensity, the NPs concentration, and the viscosity of the medium has been evaluated and compared to the reference system. This has been done by preparing three samples, each of which differs by only one parameter from the reference one as reported in Table 1: (i) in the first one, the applied magnetic field has been reduced to 6 mT (60Eb40BA\_3NPs\_6mT), (ii) in the second one, the concentration of the magnetic fillers has been reduced to 0.5 wt.% (60Eb40BA\_0.5NPs\_30mT), and (iii) in the third one, the formulation has been modified to 67Eb33BA\_3NPs\_30mT to increase the viscosity up to 0.08 Pa s. The complete evaluation of how the system evolves when the experimental parameters are changed is reported in Figure S4.



**Table 1:** Viscosity, NPs concentration of the prepared formulations, and magnetic field intensity adopted to investigate the self-assembly process by optical microscopy. Compared to reference, modified values of the parameters are bold.

System	Viscosity [Pa s]	NPs [wt.%]	Magnetic Field [mT]
60Eb40BA_3NPs_30mT	0.05	3	30
60Eb40BA_3NPs_6mT	0.05	3	<b>6</b>
60Eb40BA_0.5NPs_30mT	0.05	<b>0.5</b>	30
67Eb33BA_3NPs_30mT	<b>0.08</b>	3	30

The kinetics of the chains formation for the four configurations are illustrated in Figure 3, where the time evolution of their average length-to-width (L/W) aspect ratio is shown. Here, the reference system (60Eb40BA\_3NPs\_30mT) is represented by the black continuous line in Figure 3.a, and shows an aspect ratio at the plateau of about 4. As the magnetic field is the driving force for the self-assembly process [89-91], its influence is first analyzed. When the applied field is reduced to 6 mT, any other quantity otherwise equal, the aspect ratio of the chains (green line in Figure 3.a) is reduced to 1.2, i.e. this value is about 70 % smaller than in the reference system. As the strength of dipolar interactions between NPs scale with the intensity of the applied field, reducing  $\mathbf{B}$  weakens the interactions between the aggregates, which in turn results in shorter structures [90,92-94]. This is, in low field conditions, chains attract less efficiently surrounding aggregates in head-to-tail configuration compared to the structures formed under stronger magnetic fields. The effect of nanoparticles concentration has been evaluated by reducing the load of magnetic fillers to 0.5 wt.%, any other quantity otherwise equal. In this configuration, the aspect ratio at the plateau (red curve in Figure 3.a) is about 2.7, i.e. 30 % smaller than for the reference system. In the dipolar approximation [50,95] the magnetic potential energy  $U$  scales with the mean inter-particle distance,  $r$ , as  $U \propto r^{-3}$ . Besides  $r^3$  is approximately equal to the inverse of volume density of NPs (the fillers), such that the magnetic interaction between the particles linearly scales with the concentration the fillers, i.e.  $U \propto N$ . Consequently, in diluted systems magnetic interactions are less efficient and lead to the formation of shorter aggregates of particles [91]. The viscosity of the resin affects the mobility of the nanoparticles, and therefore the self-assembly process. Indeed, in a medium of viscosity  $\eta$ , the mobility of a filler can be written as  $k_B/(3\pi d\eta)$ , where  $k_B$  is the Boltzmann constant, and  $d$  the diameter of the NP [96]. The effect of viscosity was studied by varying the Ebecryl/butyl acrylate ratio in the formulation. For instance, decreasing the BA content to 33 wt.% in Ebecryl 8232 resin (67Eb33BA), the viscosity increases from 0.05 Pa s to 0.08 Pa s (about 60% of increase). This results in a reduction of the kinetics of the self-assembly process

(blue curve in Figure 3.a). Indeed, the 67Eb33BA\_3NPs\_30mT system reaches the plateau-region after about 5 minutes, while the less viscous reference system reaches it in about 2 minutes. It is worth noticing that the viscosity does not change the symptomatic length of the chains, but only the time required to reach it [87]. This point is of particular importance as if the printing process starts before the plateau is reached, the final object will not have a homogeneous microstructure.

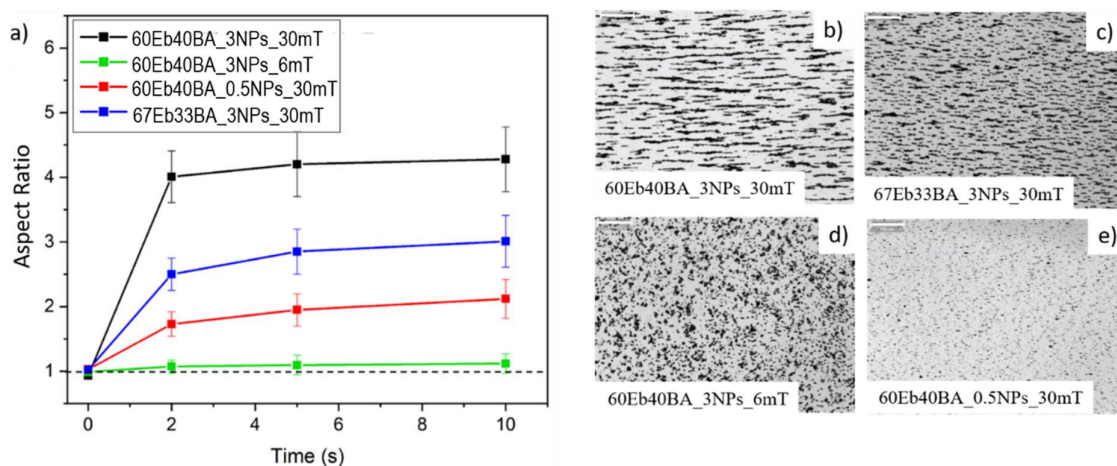


**Figure 3:** a) Length-to-width aspect ratio vs time of three samples defined in Table 1 compared to the reference values (black line). b) to e) Optical-microscopy images of the microstructures.

To precisely control the average length of the chains in each layer is the first condition to tailor the magnetic properties, for this reason the strategy here followed consists in starting to 3D print with a lag time sufficient to reach the plateau.

The magnetic microstructure can be tuned by defining in advance desired plateau value by changing the experimental parameters (applied field, viscosity, and concentration of the fillers).

### 2.3. Rotation of the magnetic chains

Beside the control of chains length, there is a second parameter that must be taken into account: the spatial orientation of the chains in each printed layer. When the applied field is rotated, the aggregates undergo a magnetic torque which forces the microstructure to rotate in order to re-orient their easy magnetic axis along the applied field [97-102]. Thus, in this section we investigate how to control the spatial orientation of the chains once they have reached their saturation length.

It is worth mentioning that the behavior of magnetic chains exposed to rotating magnetic fields has been extensively studied for magnetorheological suspensions, i.e. suspensions of micron-

sized magnetizable particles immersed in a nonmagnetic fluid, principally for stirring applications [97-102]. However, no detailed studies have been published so far for 3D printing purposes.

Exploiting the fact that the magnetic field ( $\mathbf{B}$ ) is a vector, characterized by a direction and a magnitude (or strength), we decomposed the problem into two sub-problems. Our strategy consists of first producing a magnetic field in the X-Y plane and then adding a further component of the field in the Z direction.

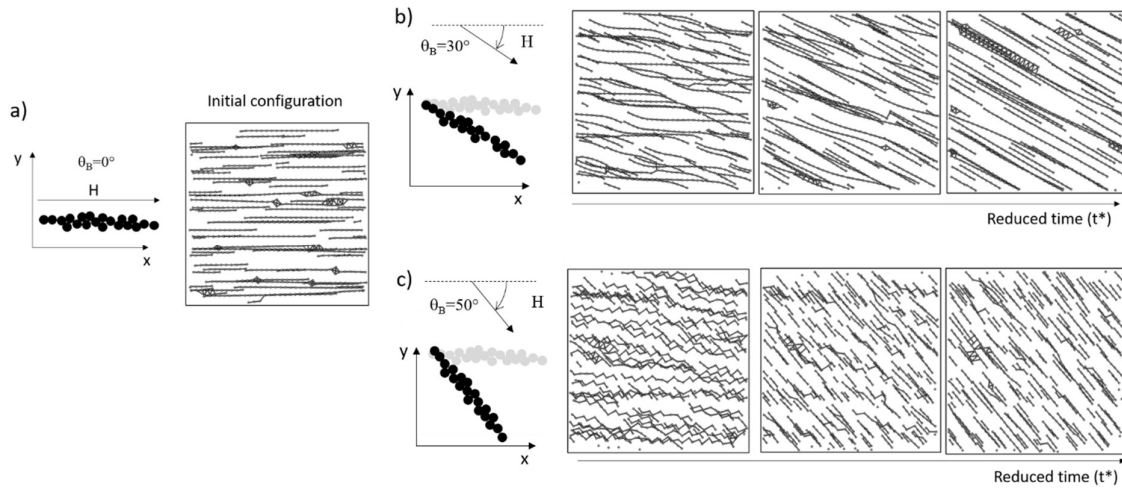
### 2.3.1. Rotation of the magnetic chains in the X-Y plane

Interesting observations have been obtained by numerical simulations (Figure 4). First, randomly distributed NPs are submitted to an external magnetic-induction parallel to the  $x$  axis to form linear chains of NPs (Figure 4.a). In this case, the energy minimization leads to the formation of linear NP chains with an average length,  $L_0$ , of  $15 \pm 3 d$  ( $1.5 \pm 0.3 \mu\text{m}$ ). In a second step, the magnetic direction was rotated around the  $z$  axis by an angle of  $\theta_B$  (see SI file for details). The mean quantities have been then obtained over six independent trajectories for each angle. Figure 4.b shows that for  $\theta_B = 30^\circ$  the extremities of the chains are the first to rotate giving at the whole structure a S-like shape. However, for longer times, chains align themselves along the field direction remaining unaltered and parallel one to another. The situation is different when the rotation angle is increased. In this case, already at the beginning of the simulation, topological instabilities develop, leading the rupture of the chains in smaller sections, which rapidly align along the direction of the applied field. The numerical simulations thus evidence two rotation regimes.

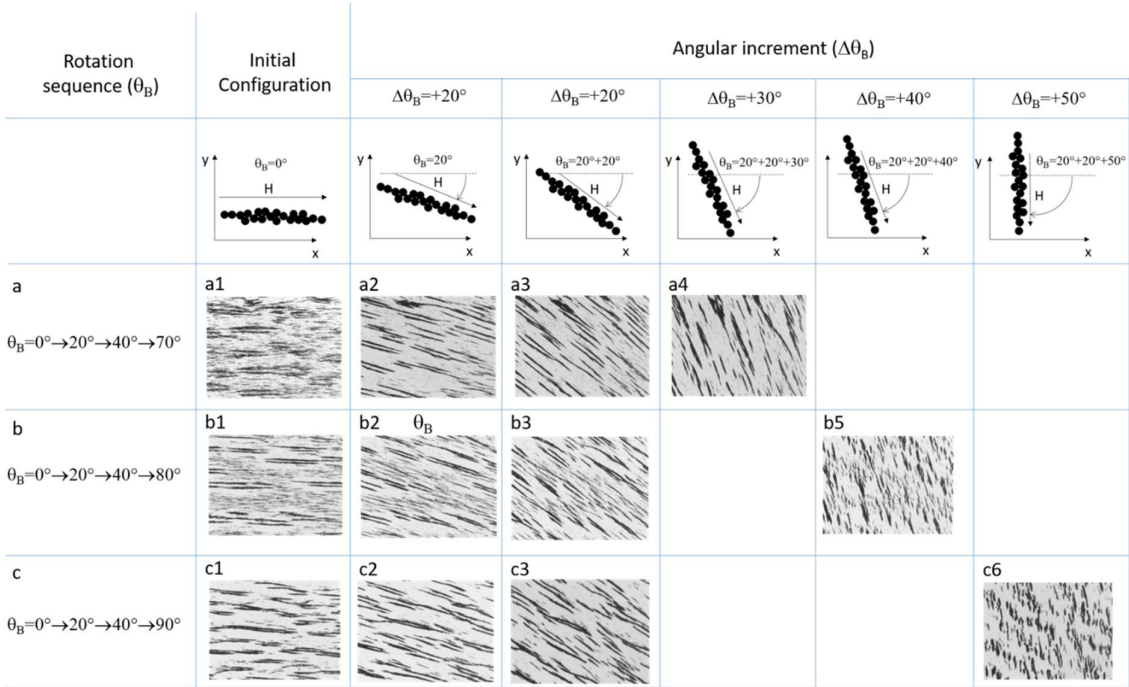
Experimentally, as described in the Experimental part and SI file, the field in the X-Y plane is controlled using a polymeric ball-bearing to which are attached NdFeB permanent magnets. Using the 60Eb40BA\_3NPs formulation as a reference, the self-assembly process is first triggered by applying a 30 mT magnetic field in the horizontal direction ( $\theta_B = 0$ ) for 10 min for the chains to reach the *plateau*. Subsequently, to mimic the spatial orientation of the microstructure during the printing process, the magnetic field is rotated by a discrete angle ( $0 \leq \theta_B < 90^\circ$ ), and each rotation step has been monitored *in situ* up to 120 seconds by optical microscopy. This time interval is roughly representative of the photo-curing process that takes place during printing step.

Figure 5 illustrates how the microstructure evolves when successive rotations of the magnetic field are applied to the system. In the first one (Figure 5 line a) two successive rotations of

$\Delta\theta_B = 20^\circ$  are followed by one of  $\Delta\theta_B = 30^\circ$ , to reach a final angle of  $\Delta\theta_B = 70^\circ$ . Here, for all the rotation angles, ( $\Delta\theta_B = 20^\circ$  and  $\Delta\theta_B = 30^\circ$ ) the chains are stable upon rotation (they do not break) while the final angular configuration ( $\theta_B = 70^\circ$ ) is reached. In Figure 5 line b, two successive rotations of  $\Delta\theta_B = 20^\circ$  are followed by one of  $\Delta\theta_B = 40^\circ$  and in Figure 5 line c by one of  $\Delta\theta_B = 50^\circ$ , respectively. Again, for the two successive rotations of  $\Delta\theta_B = 20^\circ$  the chains remain intact, whereas for larger rotation angles, see for instance Figure 5 case b5 ( $\Delta\theta_B = 40^\circ$ ) and Figure 5 case c6 ( $\Delta\theta_B = 50^\circ$ ), chains disaggregate into smaller fragments which align themselves to the field direction. This confirms that the microstructure is not stable for every rotation angle and that two regimes exist. This is, when the angular increment  $\Delta\theta_B$  is smaller than about  $30^\circ$  the system is stable and the microstructure is maintained, whereas for larger values,  $\Delta\theta_B > 40^\circ$ , some instabilities appear that favor the rupture of the chains leading to the formation of smaller ones.



**Figure 4:** Numerical simulations showing the evolution of a) already formed chains along the x-axis ( $\theta_B = 0$ ), for two different rotation angles of the applied magnetic field, i. e. b)  $\theta_B = 30^\circ$ , and c)  $\theta_B = 50^\circ$ . For  $\theta_B = 30^\circ$  chains are stable upon rotation, whereas for  $\theta_B = 50^\circ$  they first break into smaller structure and then align themselves along the field direction. The reduced time is defined in section 1 of SI.



**Figure 5:** Time-frame evolution of the initial microstructure (10 min and  $\mathbf{B}=30$  mT) for different rotation sequences.

As the variation of the average lengths of the chains can modify both the magnetic response of printed object and its mechanical properties, this point has been investigated in more details by studying both the evolution of the mean length of the chains, and their rotation angle.

Figure 6.a shows the experimental time evolution of the normalized chains' length ( $L/L_0$ ) for two cases: i.e. a rotation of  $\theta_B = 30^\circ$  and one of  $\theta_B = 45^\circ$ .  $L_0$  is the initial average length of the chains, i.e. 10 min after the application of the magnetic field, and  $L$  their average length at the time  $t$ . For  $\theta_B = 30^\circ$  (full circles), after a small shrinking of about 10% observed at the beginning of the process, the length of the chains remained almost constant for the duration of the experiment. Conversely, when the rotation angle is set to  $\theta_B = 45^\circ$  (open circles) the  $L/L_0$  ratio drops of about 50 % within the first 30 seconds of rotation. This clearly indicates the existence of two different angular-dependent regimes. The ensemble of the experimental results has been checked for longer times and for more rotation angles using numerical simulations. Figure 6.b shows that the mean NP chains length decreases at the beginning of the rotation, and then for longer time recover a value close to the initial one. The maximum decrease of the length,  $\Delta L$ , exhibits an abrupt variation between  $\theta_B = 30^\circ$  and  $\theta_B = 40^\circ$  evidencing the existence of two regimes. The angular dependence of  $\Delta L$  has been investigated in more detail in Figure 6.c. In the first regime, corresponding to  $\theta_B < 30^\circ$ , a small reduction of the chains'

length is observed, which linearly depends on the rotation angle  $\theta_B$ . On the contrary, for larger rotation angles,  $\theta_B > 40^\circ$ ,  $\Delta L$  is much larger and almost independent on the value of  $\theta_B$  (Regime II). This means that the NP chains break during the rotation and reconstruct less easily for angles  $\theta_B > 40^\circ$ .

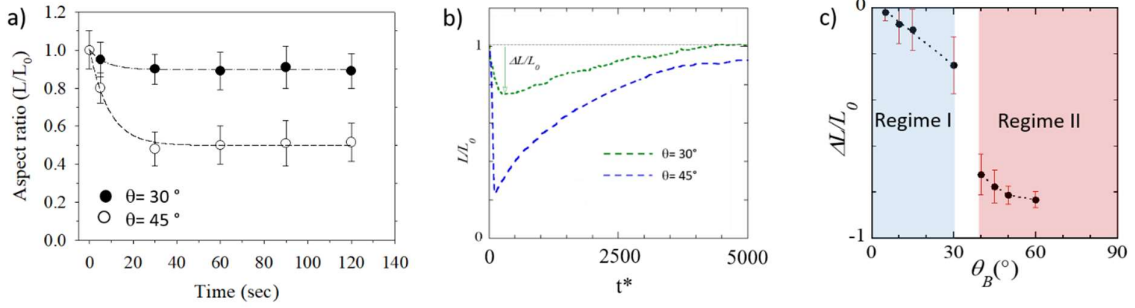


**Figure 6:** a) Experimental and b) numerical temporal evolution of the ratio  $L/L_0$  of the chains for two rotation angles. c) Numerical angular dependence of the normalized maximum-decrease of the chains' length,  $\Delta L/L_0$ . The two regimes (I and II) are painted in blue and red, respectively. The reduced time is defined in section 1 of SI.

### 2.3.2 Evolution of the rotation angle

The rotation kinetics has been experimentally investigated in Regime I by considering four different rotation angles:  $5^\circ$ ,  $10^\circ$ ,  $15^\circ$ , and  $30^\circ$ , Figure 7.a. Although, all the curves show the same behavior, i.e. a rapid rotation toward a plateau region, the slope of the curves and the height of plateau depend on the rotation angle. This is, the larger the imposed angle, the smaller the initial slope and the slower the rotation process. Otherwise stated, the larger the rotation angle, the longer the time is required for the chains to reach the nominal value. This is shown in Figure 7.b where the “angular gap” to reach the nominal rotation, i.e. the value of 1, measured at 120 sec, is observed to linearly scale with the applied rotation angle. This observation has been confirmed by numerical simulations, that have been also used to study what happens in regime II, i.e. for angles  $\theta_B > 40^\circ$ , Figure 7.c. In this second regime, where chains break in smaller pieces, the mean rotation angle rapidly reach the nominal value  $\theta_B > 40^\circ$ . This is more clearly evidenced in Figure 7.d, where in regime II the “angular gap” measured at a reduced time  $t^* = 2500$  remains close to zero for all the measured angles in contrast with the behavior in regime I.

To conclude, in regime I, where the chains do not break and are thus longer, the larger the imposed the rotation, the longer the time necessary to reach the nominal angle. Conversely, in

regime II, where the chains break and are thus shorter, the rotation process is faster and independent on the nominal angle.

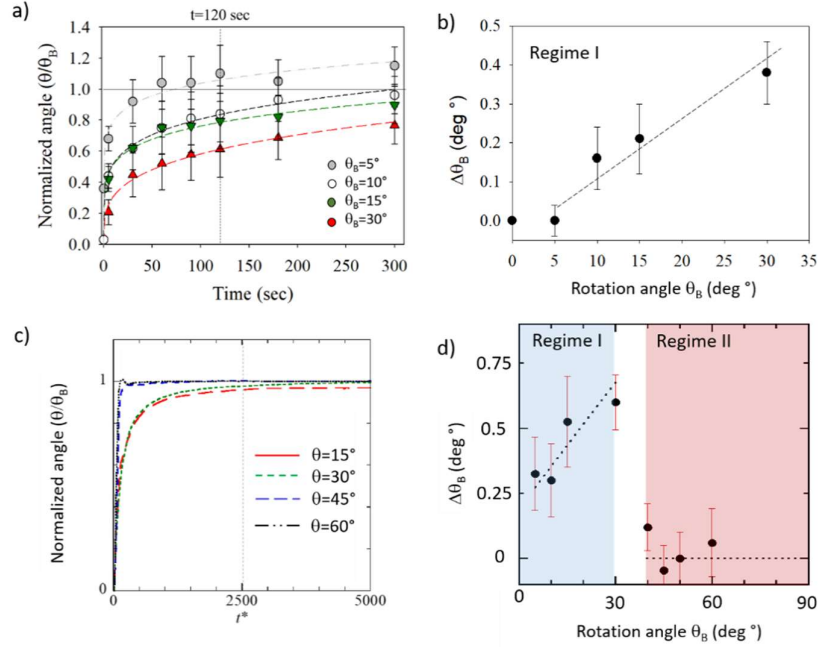


**Figure 7:** a) experimental rotation of the chains for different rotation angles in regime I, i.e.  $\theta_B < 30^\circ$ . The nominal value, i.e.  $\theta/\theta_B = 1$ , is indicated by the gray line. b) the measure angular gap  $\Delta\theta_B$  compared to the nominal one as measured at 120 sec after the application of the magnetic field. c) numerical simulations for rotation angles up to  $\theta_B = 60^\circ$ . d) Simulated evolution of the angular gap in regimes I and II at  $t^* = 2500$ . The reduced time is defined in section 1 of SI.

### 2.3.3 Physical mechanism for the existence of two regimes

The existence of the two regimes can be explained simulating a chain composed of two NPs and by computing the forces, parallel and perpendicular to the chain's axis, acting on one of the two NPs (Figure 8.a, the model is described in SI). The parallel force is attractive between the NPs, decreases from  $\theta_B = 0$  and then becomes repulsive for an angle greater than  $57^\circ$ . The perpendicular force module, increasing and reaching a maximum at  $\theta_B = 45^\circ$ , leads to a maximum value of the rotational force. From the static point of view, the two NPs chains become unstable for  $\theta_B > 57^\circ$ . This defines two regimes for the behavior of NPs. In regime I, the NPs remain bounded, whereas in regime II they separate. In a dynamical simulation, a centrifugal force is added to the parallel force and enhance the separation of the two NPs. It results that the critical angle of  $57^\circ$  should be significantly reduced.

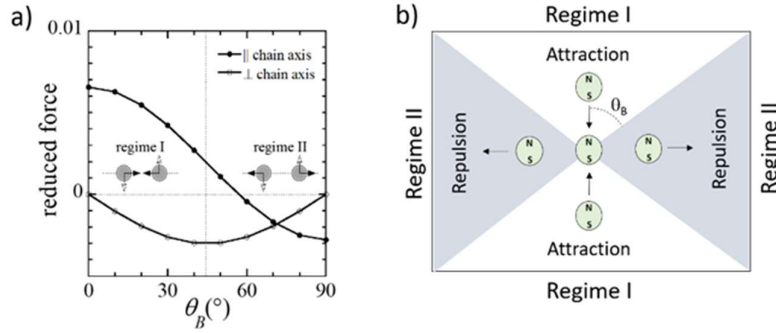


**Figure 8:** a) Parallel and perpendicular reduced forces as a function of the  $\theta_B$  angle in the case of a two NPs chain. The two curves refer to the left NP. The  $\theta_B$  angle is statically applied on the chain aligned along the x axis ( $\theta_B = 0$ ). The black and white arrows correspond to parallel and perpendicular forces undergone by the NPs, respectively. b) Schematic representation of the two regimes.

In this section, we have seen that the orientation of the chains is not a straightforward process, and that the chains either can whole rotate (regime I) or can break into smaller parts (regime II), depending on the applied angle. In addition, the kinetics at which the chains align to the new magnetic orientation is  $\theta_B$  dependent. For the sake of clarity this behavior is sketched in Figure 8.b.

As final remark, theoretical simulations confirm that for 3D printing processes in which in two consecutive layers is expected to have chains with an orientation difference greater than  $30^\circ$ , multiple steps with rotation angles lower than  $30^\circ$  should be performed to not lose the microstructure, as also experimentally illustrated in Figure 5.

### 2.3.4. Control the orientation of magnetic chains in the whole space

The control of the orientation of the magnetic chains' in the Z-axis is the last step to achieve the full programmability of the microstructures during the printing process. To produce a magnetic field in z-direction a solenoid has been used, which is coupled to the ball-bearing as shown in Figure 9.a. The formation and the spatial evolution of the magnetic chains as a function of the orientation and the intensity of the applied induction field  $\mathbf{B}$  are shown in Figure 9.b-h. Figure 9.b represents the as-deposited formulation, where neither permanent magnets nor the solenoid were used. In this case, fillers are homogeneously distributed within the resin. This corresponds to the initial configuration of the printable resin. First, self-assembled chains of vertically oriented NPs were obtained (Figure 9.c). This was done by activating only the



solenoid to generate a magnetic field of 10 mT. Because the optical axis of the microscope coincides with the magnetic Z-axis produced by the solenoid, the image is composed by an ensemble of circular spots, each of which represents the projection of the vertically-aligned chain on the X-Y plane. Next, permanent magnets were introduced to increase the magnetic field in the X-Y plane up to 5 mT (Figure 9.d). This results in the rotation of the magnetic vector from the Z-axis, which is followed by the spatial rotation of the magnetic chains, as shown in Figure 9.c. The latter point is experimentally confirmed by the fact in the projected image of the chains is longer than in the previous case (Figure 9.c). Then, the magnetic field in the X-Y plane was increased further increased up to 10 mT (Figure 9.e). Again, the magnetic chains appear longer, indicating that they were much more inclined on the X-Y plane. At this point, the field in the Z direction has been put to zero ( $B_z = 0$ ) by switching off the solenoid. In this configuration, magnetic chains are aligned in the X-Y plane (Figure 9.f). To verify the reversibility of the process, the permanent magnets were removed, and the solenoid was again activated at 10 mT to obtain vertically oriented chains (Figure 9.g). To conclude, the horizontal configuration was again achieved by inserting the magnets and switching off the solenoid (Figure 9.h).

The optical images validate our experimental approach demonstrating the good programmability of the microstructure within the photo-curable resin in the whole X-Y-Z space. Indeed, by varying the rotation of the ball bearing and controlling the voltage supplied to the solenoid, it was possible to tune the dimensions and direction of the magnetic chains. It is thus in principle possible to reproduce the same process in each printed layer and to fabricate a 3D printed material characterized by complex and spatially oriented microstructures. The magnetic forces and torques associated with the complex magnetic anisotropies would allow to enhance the actuation control on the 3D printed magnetic polymers, exploiting different types of movements within the same object. The final step will be thus the modification of the 3D printer to integrate this setup. This will be described in the next section.

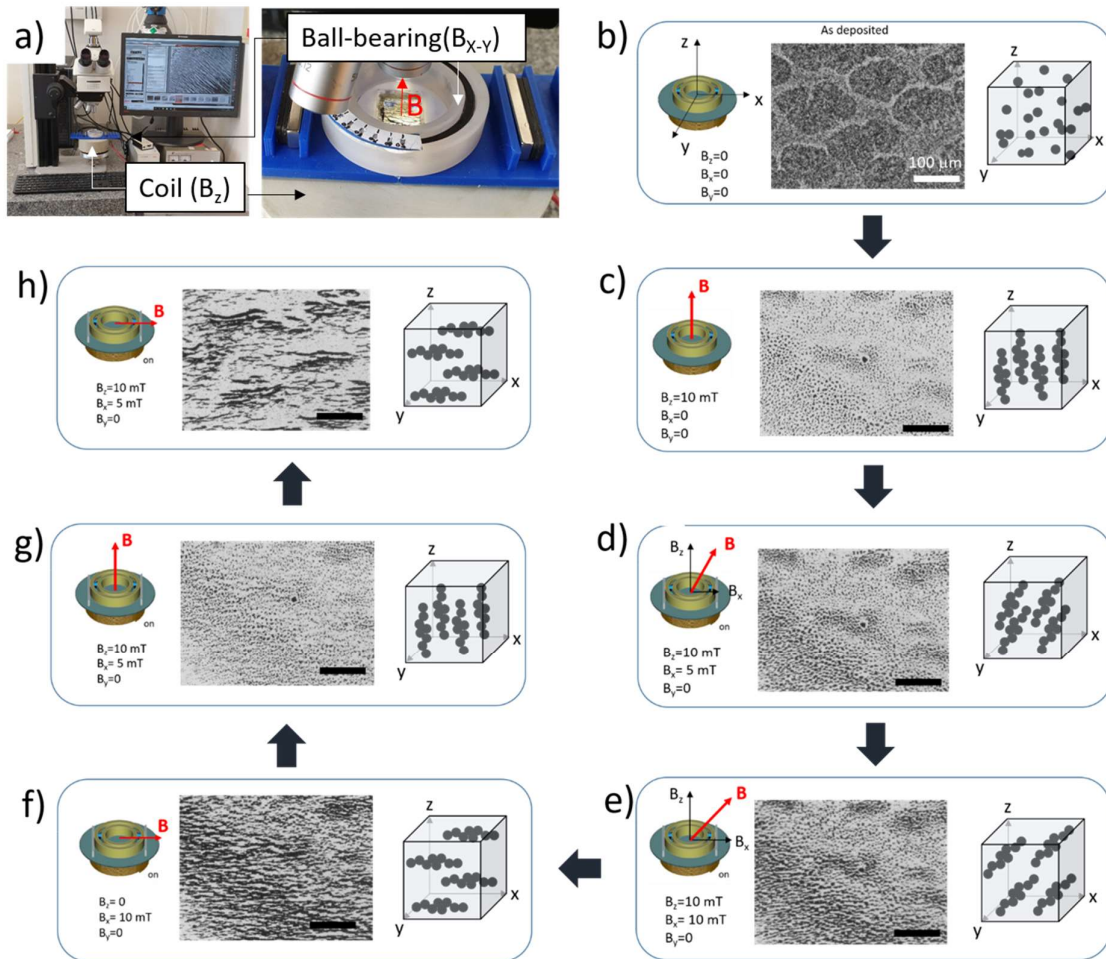


**Figure 9:** Programming of the spatial magnetic chains' orientation by tuning the magnetic field intensity generated by the solenoid and corresponding optical microscopy image.

## 2.4 Controlling the hierarchical microstructure in a magneto-responsive polymer using a commercial DLP 3D printer: a proof of concept

In previous sections we described the landscape allowing to control the microstructure within a photo-curable resin, i.e. the chains' average length, their spatial orientation, and their stability upon rotation. Here, we applied this knowledge to print magneto-responsive polymers possessing hierarchical microstructure, i.e. where in each printed layer the chains of NPs have their own spatial orientation. This has been done by developing an experimental set up that does not necessitate neither a complicate nor an expensive solution and that can be, in principle, implemented to all the existing *open source* DLP printers. Thus, a commercially available DLP printer, a RobotFactory HD 2.0, was modified to this purpose as described in SI.

The adopted solution is based on the use of a rotating ball bearing, onto which permanent magnets are attached. The final set-up of the modified DLP apparatus is reported in Figure 10. As the ball bearing is fixed onto the glass plate of the vat of the DLP printer, it becomes by construction the new resin reservoir (Figure 10.a). This set-up avoids light interactions between the projector and the ball bearing, maintaining the original quality and resolution of the printer (Figures 10.b-d). The direction of the applied field is controlled by rotating the external wall of the ball bearing, and it is activated using a printed linear-to-rotary actuator controlled by an Arduino microcontroller, (Figures 10.b and 10.e, Figure S8 and Video S1 in operation).

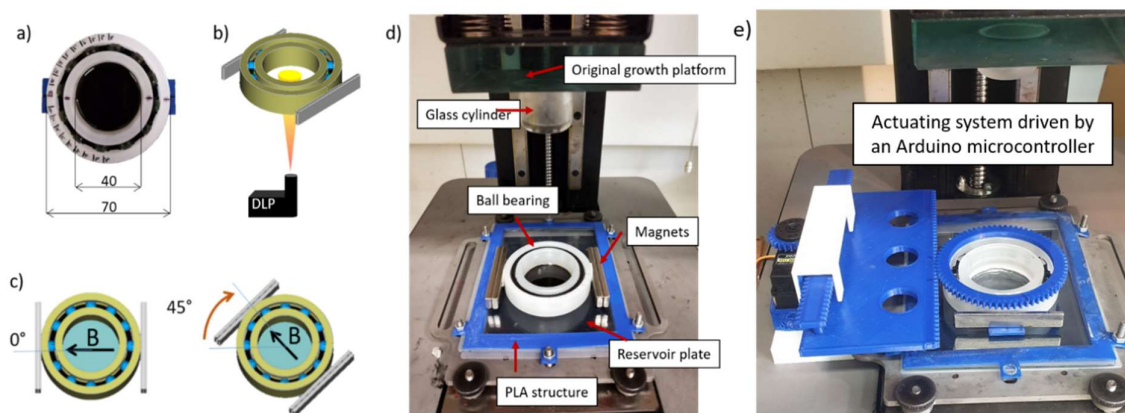


**Figure 10:** The ball bearing used to apply controlled magnetic field during the printing process. b) The developed set-up allows the passage of the light coming from the projector of the printer. c) The direction of the applied field is controlled by rotating the external wall of the ball bearing. d-e) Final appearance of the modified DLP printer.

### 2.5 3D printed magneto-responsive pyramid with hierarcical microstructure

As a proof of concept, a pyramid-like three-level structure was 3D printed to validate the proposed magnetically assisted 3D printing, Figure 11.a. For each planar floor of the pyramid, the direction of the magnetic field was changed by remotely rotating the external wall of the ball bearing such that three different chains orientations were obtained (Experimental Section), Figures 12.b-c. To facilitate optical microscopy investigations on the microstructure, the load of magnetite nanoparticles was limited to 0.5 wt.%. Two formulations differing by one order of magnitude in viscosity (0.18 Pa s, and 0.02 Pa s) were used to 3D print and compare the microstructure of the objects.

The optical microscope images (Figures 11.d and 11.e) demonstrate that the proposed DLP printer set-up enables the possibility to induce magnetic particles self-assembly in the photocurable resins and to incorporate the assembled microstructure within the printed layers of the objects. Furthermore, the magnetic chains embedded in the more viscous formulation are shorter than those

observed in the less viscous one. This demonstrates that it is possible to predict the dimensions of the aggregates controlling the viscosity of the formulation, and these results are in good agreement with the optical microscopy observations.

Besides the dimension of the aggregates, the modified DLP printer is also effective in controlling their orientation. As reported in Figures 12.d-e the direction of the assembled chains is consistent with the direction of application of the magnetic field used to print the objects. No remarkable differences in terms of chains orientation were observed for the two objects, proving that, as already observed by optical microscopy, in this range of viscosity the rotation of the chains is not influenced by the medium.

These results demonstrate that the proposed modification set-up of a DLP printer allows to embed self-assembled magnetic chains in the polymeric matrix, and to control the orientation of the aggregates in each printed layer, achieving a full micro-structuration of the whole composite material.

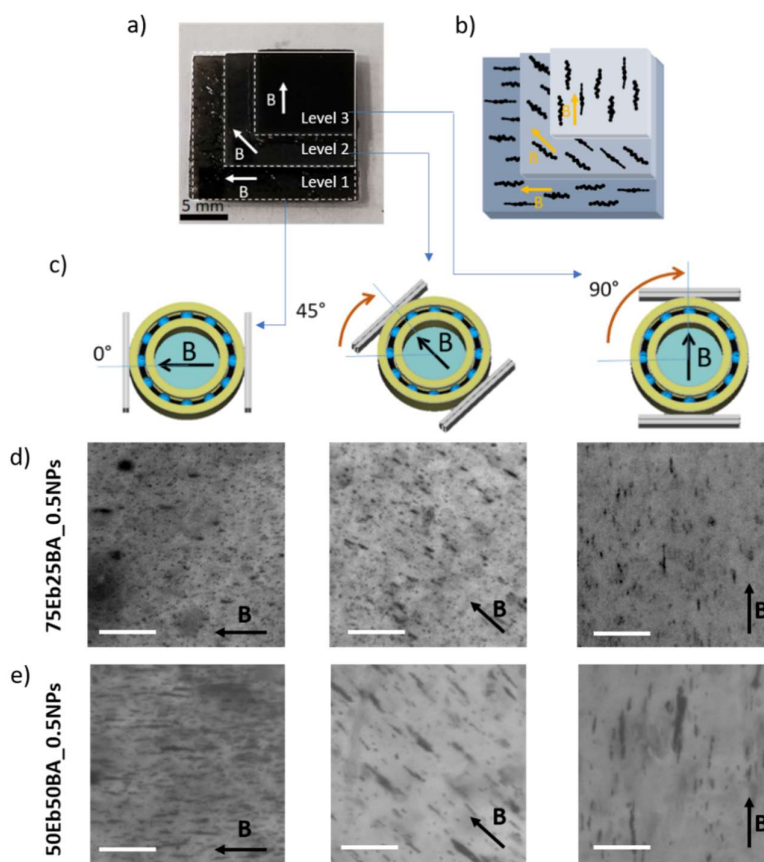


**Figure 11:** a) Photograph of DLP 3D printed object with three different orientations of nanoparticles chains (thickness of each level 500  $\mu\text{m}$ . b) sketch of the programmed orientations of the chains in the 3D printed object. c) sketch showing the orientation of the magnets used to obtain each level in the structure with oriented magnetic

chains (0°, 45°, and 90°). Corresponding optical microscope images of the microstructures observed in the printed objects for d) 75Eb25BA\_05NPs and for e) 50Eb50BA\_05NPs formulations. The scale bar is 100 µm.

### 3. Conclusions

In this work, we report an easy and accessible route to take advantage of the self-assembly process of magnetic particles to program the microstructure of DLP printed composite polymers. First, the microstructure of a single layer was investigated by controlling different parameters such as viscosity, intensity of magnetic field and exposure time.

Optical microscopy investigations and numerical simulations were carried out to define the programming of the microstructures by dispersing Fe<sub>3</sub>O<sub>4</sub> NPs in acrylic photocurable resins. Both the field intensity and the NPs concentration promote the formation of longer chains. Instead, an increase in the viscosity of the system postpones the saturation of the self-assembly process leading to shorter aggregates. The direction of the chains was programmed in each printed layer by controlling the applied magnetic field. Two rotational regimes of the chains were found according to the amplitude of their rotation.

All these data allowed a complete understanding of the phenomena, in order to define the local microstructure of a 3D printed component. A commercial DLP printer was modified by implementing a ball-bearing-permanent magnets module in the resin reservoir to apply controlled magnetic fields during the printing process.

3D-printed objects with programmed microstructures were fabricated, and the results were in good agreement with the optical microscopy investigations and the theoretical model.

The possibility to combine highly resolute materials with programmed and predictable microstructures by a 3D printing methodology can enable to take advantage of particular magnetic and mechanical properties of magneto-responsive polymers. This opens the way to further achievements in several application fields such as soft-robotics, actuators, and sensors, which will be presented in future reports.

### 4. Experimental Section/Methods

*Materials:* Ebecryl 8232 (Eb), a commercial urethane-acrylate resin, was kindly provided by Allnex. As a reactive diluent, Butyl Acrylate (BA) was purchased from Merck and added in different ratios to Eb to tune the viscosity of the formulations. Spherical magnetite (Fe<sub>3</sub>O<sub>4</sub>) nanoparticle (NPs) with a nominal diameter ranging from 50 to 100 nm (Merck, used as received) were added to the photocurable resins as the magnetic fillers. As the radical photoinitiator (PIr), Phenylbis(2,4,6-trimethylbenzoyl)phosphine oxide (Merck) was added to the 3D printable formulations at 1 wt.%.

Using a FlashForge creator on Pro FFF printer, a commercially available 1.75 mm PLA filament is used to fabricate the different parts of the modified DLP printer.

*Formulation Preparation:* Formulation containing the 60wt.% of Eb, 40wt.% of BA and 3wt.% of Fe<sub>3</sub>O<sub>4</sub>NPs (60Eb40BA\_3NPs) was used as reference for the optical microscopy investigations of the self-assembly process of NPs and the rotation of the magnetic chains. To evaluate the effect of the material characteristics on the dimensions of the assembled chains, other two formulations were prepared: 67Eb33BA\_3NPs for viscosity, 60Eb40BA\_0.5NPs for NPs concentration.

Formulations with the 25wt.% and 50wt.% of BA, 1phr of photoinitiator, and 0.5 wt.% of NPs were 3D printed (75Eb25BA\_0.5NPs and 50Eb50BA\_0.5NPs respectively). The compositions of the tested formulations are resumed in Table 2. Before use, all the formulations were homogenized by mechanical stirring with IKA Ultraturrax for 10 minutes at 25000 rpm, followed by 5 minutes of sonication at room temperature.

**Table 2:** Composition of the tested and 3D printed formulations.

Formulation	Ebecryl 8232 [wt.%]	Butyl acrylate [wt.%]	Fe <sub>3</sub> O <sub>4</sub> NPs [phr]	PIr [phr]
<i>Optical microscopy</i>				
60Eb40BA_0.5NPs	60	40	0.5	/
60Eb40BA_3NPs	60	40	3	/
67Eb33BA_3NPs	67	33	3	/
<i>3D printing</i>				
75Eb25BA_0.5NPs	75	25	0.5	1
50Eb50BA_0.5NPs	50	50	0.5	1

*Optical Microscopy Sample Preparation:* For the optical microscopy investigations, a drop of formulation was coated on a microscope slide and coated with a wire-wound bar obtaining a film thickness of about 200 μm. The optimum conditions to detect the aggregates were obtained by dispersing the 3phr of Fe<sub>3</sub>O<sub>4</sub> particles in 60Eb40BA formulation (viscosity,  $\eta=0.05$  Pa s measure with Anton-Paar rheometer).

*3D Printer Modifications:* The ball bearing was purchased from SKF, and its case is made of nylon and its balls in glass. It is 10 mm thick with an external diameter of 70 mm, whereas the diameter of the central cavity is 40 mm. Magnetic field was applied using a pair of NdFeB permanent magnets purchased on Supermagnete.com. The magnetic polarization was along the

shorter dimension Two different  $\text{Nd}_2\text{Fe}_{14}\text{B}$  magnets have been used: the dimensions of the A magnet are 60x10x2 mm, and those of the B magnet 40x10x4 mm. Their magnet grade is N45 and their average properties are: residual induction 1350 mT, coercivity  $12 \times 10^3$  Oe, Curie temperature 310 °C. The fields at the surface measured using a HFBTE SJ700 Gaussmeter are 120mT and 310 mT for magnet A and B, respectively. The magnetic field applied during the printing process was 10 mT. The PLA structure designed to maintain fixed the resin reservoir was 3D printed using an FFF 3D printer (FlashForge Creator Pro). As the new growth platform, a custom glass cylinder with a diameter of 25 mm and a height of 40 mm was crafted and glued to the original platform. More details in SI file.

*3D-Printed Sample Preparation:* The formulations were 3D printed with the modified RobotFactory HD 2.0 DLP printer. The optics of the printer were not modified, it is equipped with a projector emitting in the visible light range with an intensity of  $10 \text{ mW cm}^{-2}$ . Different rotation angles of the magnets were used  $0^\circ$ ,  $45^\circ$ , and  $90^\circ$ . The thickness of each planar floor was 500  $\mu\text{m}$ , sliced into 10 sub-layers, each 50  $\mu\text{m}$  thick. Printing parameters are based on previous work [84], with 2.5 s of irradiation for base layers and 1.2 s of irradiation for the structure, layer thickness 50  $\mu\text{m}$ . After printing the samples were cleaned in ethanol and UV post-cured for 10 minutes by a medium-pressure mercury lamp also provided by RobotFactory.

*Characterizations:* An Anton Paar rheometer (Physica MCR 302) was used to perform rheological tests. The gap between the plates was settled at 0.2 mm, and the shear rate was varied from 0.1 to  $100 \text{ s}^{-1}$ . Optical microscopy observations were performed with a Leica DM 2500 m equipped with a camera to follow in situ the evolution of the tested systems. The objective lenses had 2.5x magnification. The observations were taken by the transmitted light microscopy method to enhance the contrast and avoid light reflection. Image analysis was performed with ImageJ software approximating the aggregates to ellipses. Similarly to other image analysis method reported in the literature [100-102], the images were transformed in grey-scale and the magnetic chains were approximated to ellipses and their length and width were measured in terms of pixels and then reported to physical units by the scale bar. Further details on the image analysis method are reported in the Supporting Information of this work.

*Magnetic Testing* During the testing, the magnetic field was applied using a pair of NdFeB permanent magnets, described above. Varying the typology of magnets and their distance, the magnetic field intensity was varied between 6 and 30 mT. (see SI file). The fields are measured using a HFBTE SJ700 Gaussmeter. For experiments with rotating field, the magnets were set at eight rotation angles relative to x axis:  $5^\circ$ ,  $10^\circ$ ,  $15^\circ$ ,  $30^\circ$ ,  $40^\circ$ ,  $45^\circ$ ,  $50^\circ$  and  $60^\circ$ . An electromagnet was used to control of the orientation of the magnetic chains' in the Z-axis. For our

purposes, we used an electromagnetic lens from an electron transmission microscope (Philips CM30). The internal diameter of the lens is 45 mm, the external one 130mm, whereas the height was measured to be 40 mm. When the maximum voltage and current were supplied (~25 V and 2.5 A) the magnetic field intensity measured at the top of the solenoid was about 50 mT, i.e. ten times larger than the value usually obtained using standard Helmholtz coils. For our experiments, 10 mT were generated using a current of 1.8 A and a tension of 10 V.

### **Acknowledgements**

This work was supported by Compagnia di San Paolo through the “Joint Project with Top Universities” grant. This work has benefited from the financial support of the LabEx LaSIPS (ANR-10-LABX-0032-LaSIPS) managed by the French National Research Agency under the “Investissements d’avenir” program (ANR-11-IDEX-0003-02). This work was also performed using HPC resources from École Polytechnique through the LLR-LSI project and from the “Mésocentre” computing center of CentraleSupélec and École Normale Supérieure Paris-Saclay supported by CNRS and Région Île-de-France (<http://mesocentre.centralesupelec.fr/>).

### **References**

- [1] T. Wohlers, 3D Printing and Additive Manufacturing State of the Industry. Annual Worldwide Progress Report., Wohlers Report, Exec. Summ. (2017).
- [2] B.C. Gross, J.L. Erkal, S.Y. Lockwood, C. Chen, D.M. Spence, Evaluation of 3D printing and its potential impact on biotechnology and the chemical sciences, *Anal. Chem.* 86 (2014) 3240-3252. <https://doi.org/10.1021/ac403397r>.
- [3] R. D’Aveni, The 3D Printing revolution, *Harv. Bus. Rev.* (2015). <https://hbr.org/2015/05/the-3-d-printing-revolution>.
- [4] B. Berman, 3-D printing: The new industrial revolution, *Bus. Horiz.* (2012). <https://doi.org/10.1016/j.bushor.2011.11.003>.
- [5] A. Ben-Ner, E. Siemsen, Decentralization and Localization of Production: The Organizational and Economic Consequences of Additive Manufacturing (3D Printing), *Calif. Manage. Rev.* 59(2) (2017) 5-23. <https://doi.org/10.1177/0008125617695284>.
- [6] R.D. Farahani, M. Dubé, D. Therriault, Three-Dimensional Printing of Multifunctional Nanocomposites: Manufacturing Techniques and Applications, *Adv. Mater.* 28(28) (2016) 5794-5821. <https://doi.org/10.1002/adma.201506215>.
- [7] N. Mohan, P. Senthil, S. Vinodh, N. Jayanth, A review on composite materials and



- process parameters optimisation for the fused deposition modelling process, *Virtual Phys. Prototyp.* 12(1) (2017) 47-59. <https://doi.org/10.1080/17452759.2016.1274490>.
- [8] A. Medellin, W. Du, G. Miao, J. Zou, Z. Pei, C. Ma, Vat photopolymerization 3D printing of nanocomposites: A literature review, *J. Micro Nano-Manufacturing.* 7(3) (2019) 031006. <https://doi.org/10.1115/1.4044288>.
- [9] X. Wang, M. Jiang, Z. Zhou, J. Gou, D. Hui, 3D printing of polymer matrix composites: A review and prospective, *Compos. Part B Eng.* 110 (2017) 442-458. <https://doi.org/10.1016/j.compositesb.2016.11.034>.
- [10] G. Gonzalez, A. Chiappone, I. Roppolo, E. Fantino, V. Bertana, F. Perrucci, L. Scaltrito, F. Pirri, M. Sangermano, Development of 3D printable formulations containing CNT with enhanced electrical properties, *Polymer (Guildf).* 129 (2017) 246-253. <https://doi.org/10.1016/j.polymer.2016.12.051>.
- [11] A. Chiappone, I. Roppolo, E. Naretto, E. Fantino, F. Calignano, M. Sangermano, F. Pirri, Study of graphene oxide-based 3D printable composites: Effect of the in situ reduction, *Compos. Part B Eng.* 124 (2017) 9-15. <https://doi.org/10.1016/j.compositesb.2017.05.049>.
- [12] S. Lantean, I. Roppolo, M. Sangermano, C.F. Pirri, A. Chiappone, Development of new hybrid acrylic/epoxy DLP-3D printable materials, *Inventions.* 3(2) (2018) 29. <https://doi.org/10.3390/inventions3020029>.
- [13] L.J. Tan, W. Zhu, K. Zhou, Recent Progress on Polymer Materials for Additive Manufacturing, *Adv. Funct. Mater.* 30(43) (2020) 2003062. <https://doi.org/10.1002/adfm.202003062>.
- [14] H.A. Alshahrani, Review of 4D printing materials and reinforced composites: Behaviors, applications and challenges, *J. Sci. Adv. Mater. Devices.* 6(2) (2021) 167-185. <https://doi.org/10.1016/j.jsamd.2021.03.006>.
- [15] K. Niendorf, B. Raeymaekers, Additive Manufacturing of Polymer Matrix Composite Materials with Aligned or Organized Filler Material: A Review, *Adv. Eng. Mater.* 23(4) (2021) 2001002. <https://doi.org/10.1002/adem.202001002>.
- [16] A. Mitchell, U. Lafont, M. Hołyńska, C. Semprimoschnig, Additive manufacturing — A review of 4D printing and future applications, *Addit. Manuf.* 24 (2018) 606-626. <https://doi.org/10.1016/j.addma.2018.10.038>.
- [17] J. Choi, O.C. Kwon, W. Jo, H.J. Lee, M.W. Moon, 4D printing technology: A review, *3D Print. Addit. Manuf.* 2(4) (2015) 159-167. <https://doi.org/10.1089/3dp.2015.0039>.
- [18] Z.X. Khoo, J.E.M. Teoh, Y. Liu, C.K. Chua, S. Yang, J. An, K.F. Leong, W.Y. Yeong,

- 3D printing of smart materials: A review on recent progresses in 4D printing, *Virtual Phys. Prototyp.* 10(3) (2015) 103-122.  
<https://doi.org/10.1080/17452759.2015.1097054>.
- [19] R. Bogue, Smart materials: A review of recent developments, *Assem. Autom.* 32(1) (2012) 3-7. <https://doi.org/10.1108/01445151211198674>.
- [20] D.G. Shin, T.H. Kim, D.E. Kim, Review of 4D printing materials and their properties, *Int. J. Precis. Eng. Manuf. - Green Technol.* 4 (2017) 349-357.  
<https://doi.org/10.1007/s40684-017-0040-z>.
- [21] S.Y. Hann, H. Cui, M. Nowicki, L.G. Zhang, 4D printing soft robotics for biomedical applications, *Addit. Manuf.* 36 (2020) 101576.  
<https://doi.org/10.1016/j.addma.2020.101567>.
- [22] S.B. Kumar, J. Jeevamalar, P. Ramu, G. Suresh, K. Senthilnathan, Evaluation in 4D printing – A review, *Mater. Today Proc.* 45(2) (2020) 1433-1437.  
<https://doi.org/10.1016/j.matpr.2020.07.335>.
- [23] S. Joshi, K. Rawat, K. C. V. Rajamohan, A.T. Mathew, K. Koziol, V. Kumar Thakur, B. A.S.S, 4D printing of materials for the future: Opportunities and challenges, *Appl. Mater. Today.* 18 (2020) 100490. <https://doi.org/10.1016/j.apmt.2019.100490>.
- [24] H. Meng, G. Li, A review of stimuli-responsive shape memory polymer composites, *Polymer (Guildf).* 54(9) (2013) 2199-2221.  
<https://doi.org/10.1016/j.polymer.2013.02.023>.
- [25] Y. Dong, S. Wang, Y. Ke, L. Ding, X. Zeng, S. Magdassi, Y. Long, 4D Printed Hydrogels: Fabrication, Materials, and Applications, *Adv. Mater. Technol.* 5(6) (2020) 2000034. <https://doi.org/10.1002/admt.202000034>.
- [26] H. Yang, W.R. Leow, T. Wang, J. Wang, J. Yu, K. He, D. Qi, C. Wan, X. Chen, 3D Printed Photoresponsive Devices Based on Shape Memory Composites, *Adv. Mater.* 29(33) (2017) 1701627. <https://doi.org/10.1002/adma.201701627>.
- [27] H. Jiang, S. Kelch, A. Lendlein, Polymers move in response to light, *Adv. Mater.* 18(11) (2006) 1471-1475. <https://doi.org/10.1002/adma.200502266>.
- [28] I. Roppolo, A. Chiappone, A. Angelini, S. Stassi, F. Frascella, C.F. Pirri, C. Ricciardi, E. Descrovi, 3D printable light-responsive polymers, *Mater. Horizons.* 4 (2017) 396-401. <https://doi.org/10.1039/c7mh00072c>.
- [29] J. Wu, C. Yuan, Z. Ding, M. Isakov, Y. Mao, T. Wang, M.L. Dunn, H.J. Qi, Multi-shape active composites by 3D printing of digital shape memory polymers, *Sci. Rep.* 6 (2016) 24224. <https://doi.org/10.1038/srep24224>.

- [30] K. Yu, A. Ritchie, Y. Mao, M.L. Dunn, H.J. Qi, Controlled Sequential Shape Changing Components by 3D Printing of Shape Memory Polymer Multimaterials, in: *Procedia IUTAM*, 12 (2015) 193-203. <https://doi.org/10.1016/j.piutam.2014.12.021>.
- [31] Y. Mao, K. Yu, M.S. Isakov, J. Wu, M.L. Dunn, H. Jerry Qi, Sequential Self-Folding Structures by 3D Printed Digital Shape Memory Polymers, *Sci. Rep.* 5 (2015) 13616. <https://doi.org/10.1038/srep13616>.
- [32] S.E. Bakarich, R. Gorkin, M. In Het Panhuis, G.M. Spinks, 4D printing with mechanically robust, thermally actuating hydrogels, *Macromol. Rapid Commun.* 36(12) (2015) 1211-1217. <https://doi.org/10.1002/marc.201500079>.
- [33] I.T. Garces, C. Ayrançi, Advances in additive manufacturing of shape memory polymer composites, *Rapid Prototyp. J.* 27(2) (2021) 379-398. <https://doi.org/10.1108/RPJ-07-2020-0174>.
- [34] M. Layani, X. Wang, S. Magdassi, Novel Materials for 3D Printing by Photopolymerization, *Adv. Mater.* 30(41) (2018) 1706344. <https://doi.org/10.1002/adma.201706344>.
- [35] Y. Bar-Cohen, Electroactive polymers as artificial muscles: A review, *J. Spacecr. Rockets.* 39(6) (2002) 822-827. <https://doi.org/10.2514/2.3902>.
- [36] T. Mirfakhrai, J.D.W. Madden, R.H. Baughman, Polymer artificial muscles, *Mater. Today.* 10(4) (2007) 30-38. [https://doi.org/10.1016/S1369-7021\(07\)70048-2](https://doi.org/10.1016/S1369-7021(07)70048-2).
- [37] S. Bose, S. Vahabzadeh, A. Bandyopadhyay, Bone tissue engineering using 3D printing, *Mater. Today.* 16(12) (2013) 496-504. <https://doi.org/10.1016/j.mattod.2013.11.017>.
- [38] X. Zhang, P. Yang, Y. Dai, P. Ma, X. Li, Z. Cheng, Z. Hou, X. Kang, C. Li, J. Lin, Multifunctional up-converting nanocomposites with smart polymer brushes gated mesopores for cell imaging and thermo/pH dual-responsive drug controlled release, *Adv. Funct. Mater.* 23(33) (2013) 4067-4078. <https://doi.org/10.1002/adfm.201300136>.
- [39] F. Qiu, B.J. Nelson, Magnetic Helical Micro- and Nanorobots: Toward Their Biomedical Applications, *Engineering.* 1(1) (2015) 21-26. <https://doi.org/10.15302/J-ENG-2015005>.
- [40] H. Ceylan, J. Giltinan, K. Kozielski, M. Sitti, Mobile microrobots for bioengineering applications, *Lab Chip.* 17 (2017) 1705-1724. <https://doi.org/10.1039/c7lc00064b>.
- [41] R.L. Snyder, V.Q. Nguyen, R. V. Ramanujan, Design parameters for magneto-elastic soft actuators, *Smart Mater. Struct.* 19 (2010) 055017. <https://doi.org/10.1088/0964-1726/19/5/055017>.

- [42] A.R. Khokhlov, Y. Osada, *Polymer gels and networks*, Marcel Dekker, 2002.
- [43] V. V. Sorokin, G. V. Stepanov, M. Shamonin, G.J. Monkman, A.R. Khokhlov, E.Y. Kramarenko, Hysteresis of the viscoelastic properties and the normal force in magnetically and mechanically soft magnetoactive elastomers: Effects of filler composition, strain amplitude and magnetic field, *Polymer (Guildf)*. 76 (2015) 191-202. <https://doi.org/10.1016/j.polymer.2015.08.040>.
- [44] J. Winger, M. Schümann, A. Kupka, S. Odenbach, Influence of the particle size on the magnetorheological effect of magnetorheological elastomers, *J. Magn. Magn. Mater.* 481 (2019) 176-182. <https://doi.org/10.1016/j.jmmm.2019.03.027>.
- [45] Y. Nagaoka, H. Morimoto, T. Maekawa, Ordered complex structures formed by paramagnetic particles via self-assembly under an ac/dc combined magnetic field, *Langmuir*. 27(15) (2011) 9160-9164. <https://doi.org/10.1021/la201156q>.
- [46] D.A. Rozhkov, E.S. Pyanzina, E. V. Novak, J.J. Cerdà, T. Sintès, M. Ronti, P.A. Sánchez, S.S. Kantorovich, Self-assembly of polymer-like structures of magnetic colloids: Langevin dynamics study of basic topologies, *Mol. Simul.* 44(6) (2018) 507-515. <https://doi.org/10.1080/08927022.2017.1378815>.
- [47] V.S. Zverev, M.A. Gupalo, N.J. Mauser, S.S. Kantorovich, E. V. Novak, The influence of an applied magnetic field on the clusters formed by Stockmayer supracolloidal magnetic polymers, *J. Magn. Magn. Mater.* 521 (2021) 167445. <https://doi.org/10.1016/j.jmmm.2020.167445>.
- [48] M. Ma, Q. Zhang, J. Dou, H. Zhang, D. Yin, W. Geng, Y. Zhou, Fabrication of one-dimensional Fe<sub>3</sub>O<sub>4</sub>/P(GMA-DVB) nanochains by magnetic-field-induced precipitation polymerization, *J. Colloid Interface Sci.* 374(1) (2012) 339-344. <https://doi.org/10.1016/j.jcis.2012.02.015>.
- [49] G. Bertoni, B. Torre, A. Falqui, D. Fragouli, A. Athanassiou, R. Cingolani, Nanochains formation of superparamagnetic nanoparticles, *J. Phys. Chem. C*. 115(15) (2011) 7249-7254. <https://doi.org/10.1021/jp111235n>.
- [50] D. Lorenzo, D. Fragouli, G. Bertoni, C. Innocenti, G.C. Anyfantis, P. Davide Cozzoli, R. Cingolani, A. Athanassiou, Formation and magnetic manipulation of periodically aligned microchains in thin plastic membranes, *J. Appl. Phys.* 112 (2012) 083927. <https://doi.org/10.1063/1.4759328>.
- [51] D. Fragouli, R. Buonsanti, G. Bertoni, C. Sangregorio, C. Innocenti, A. Falqui, D. Gatteschi, P.D. Cozzoli, A. Athanassiou, R. Cingolani, Dynamical formation of spatially localized arrays of aligned nanowires in plastic films with magnetic

- anisotropy, *ACS Nano*. 4(4) (2010) 1873-1878. <https://doi.org/10.1021/nn901597a>.
- [52] Y.I. Dikansky, D. V. Gladkikh, A.A. Zakinyan, A.G. Ispiryan, A.R. Zakinyan, Magnetic and structural properties of magnetic colloids with a well-developed system of magnetized aggregates, *J. Mol. Liq.* 319 (2020) 114171. <https://doi.org/10.1016/j.molliq.2020.114171>.
- [53] E. V. Novak, D.A. Rozhkov, P.A. Sanchez, S.S. Kantorovich, Self-assembly of designed supramolecular magnetic filaments of different shapes, *J. Magn. Magn. Mater.* 431 (2017) 152-156. <https://doi.org/10.1016/j.jmmm.2016.10.046>.
- [54] Z. Li, F. Yang, Y. Yin, Smart Materials by Nanoscale Magnetic Assembly, *Adv. Funct. Mater.* 30(2) (2020) 1903467. <https://doi.org/10.1002/adfm.201903467>.
- [55] R.M. Erb, J.J. Martin, R. Soheilian, C. Pan, J.R. Barber, Actuating Soft Matter with Magnetic Torque, *Adv. Funct. Mater.* 26 (2016) 3859-3880. <https://doi.org/10.1002/adfm.201504699>.
- [56] H.W. Huang, M.S. Sakar, A.J. Petruska, S. Pané, B.J. Nelson, Soft micromachines with programmable motility and morphology, *Nat. Commun.* 7 (2016) 12263. <https://doi.org/10.1038/ncomms12263>.
- [57] T. Li, J. Li, K.I. Morozov, Z. Wu, T. Xu, I. Rozen, A.M. Leshansky, L. Li, J. Wang, Highly efficient freestyle magnetic nanoswimmer, *Nano Lett.* 17(8) (2017) 5092-5098. <https://doi.org/10.1021/acs.nanolett.7b02383>.
- [58] L.K. Lagorce, O. Brand, M.G. Allen, Magnetic microactuators based on polymer magnets, *J. Microelectromechanical Syst.* 8(1) (1999) 2-9. <https://doi.org/10.1109/84.749396>.
- [59] J. Kim, S.E. Chung, S.E. Choi, H. Lee, J. Kim, S. Kwon, Programming magnetic anisotropy in polymeric microactuators, *Nat. Mater.* 10 (2011) 747-752. <https://doi.org/10.1038/nmat3090>.
- [60] Y. Zhang, Q. Wang, S. Yi, Z. Lin, C. Wang, Z. Chen, L. Jiang, 4D Printing of Magnetoactive Soft Materials for On-Demand Magnetic Actuation Transformation, *ACS Appl. Mater. Interfaces.* 13(3) (2021) 4174-4184. <https://doi.org/10.1021/acsami.0c19280>.
- [61] A.K. Bastola, M. Paudel, L. Li, Development of hybrid magnetorheological elastomers by 3D printing, *Polymer (Guildf)*. 149 (2018) 213-228. <https://doi.org/10.1016/j.polymer.2018.06.076>.
- [62] A. Hodaei, O. Akhlaghi, N. Khani, T. Aytas, D. Sezer, B. Tatli, Y.Z. Menciloglu, B. Koc, O. Akbulut, Single Additive Enables 3D Printing of Highly Loaded Iron Oxide

- Suspensions, *ACS Appl. Mater. Interfaces*. 10(11) (2018) 9873-9881.  
<https://doi.org/10.1021/acsami.8b00551>.
- [63] P- Erkoç, Y. N. Odeh, N. Alrifai, O. Zirhli, N. G. Akdoğan, B. Yıldız, I. B. Misirlioglu, O. Akdoğan, Photocurable pentaerythritol triacrylate/lithium phenyl-2,4,6-trimethylbenzoylphosphinate-based ink for extrusion-based 3D printing of magneto-responsive materials, *J. Appl. Polym. Sci.*, 137(35) (2020),  
<https://doi.org/10.1002/app.49043>
- [64] B. Khatri, K. Lappe, D. Noetzel, K. Pursche, T. Hanemann, A 3D-printable polymer-metal soft-magnetic functional composite-development and characterization, *Materials (Basel)*. 11(2) (2018) 189. <https://doi.org/10.3390/ma11020189>.
- [65] E.M. Palmero, J. Rial, J. de Vicente, J. Camarero, B. Skårman, H. Vidarsson, P.O. Larsson, A. Bollero, Development of permanent magnet MnAlC/polymer composites and flexible filament for bonding and 3D-printing technologies, *Sci. Technol. Adv. Mater.* 19(1) (2018) 465-473. <https://doi.org/10.1080/14686996.2018.1471321>.
- [66] C. Huber, C. Abert, F. Bruckner, M. Groenefeld, S. Schuschnigg, I. Teliban, C. Vogler, G. Wautischer, R. Windl, Di. Suess, 3D Printing of Polymer-Bonded Rare-Earth Magnets with a Variable Magnetic Compound Fraction for a Predefined Stray Field, *Sci. Rep.* 7 (2017) 94194. <https://doi.org/10.1038/s41598-017-09864-0>.
- [67] L.M. Bollig, P.J. Hilpisch, G.S. Mowry, B.B. Nelson-Cheeseman, 3D printed magnetic polymer composite transformers, *J. Magn. Magn. Mater.* 442 (2017) 97-101.  
<https://doi.org/10.1016/j.jmmm.2017.06.070>.
- [68] C.Yue. M. Li, Y. Liu, Y. Fang, Y. Song, M. Xu, J. Li, Three-dimensional printing of cellulose nanofibers reinforced PHB/PCL/Fe<sub>3</sub>O<sub>4</sub> magneto-responsive shape memory polymer composites with excellent mechanical properties, *Addit. Manuf.* (46) (2021) 102146. <https://doi.org/10.1016/j.addma.2021.102146>
- [69] Z. Ji, C. Yan, B. Yu, X. Wang, F. Zhou, Multimaterials 3D Printing for Free Assembly Manufacturing of Magnetic Driving Soft Actuator, *Adv. Mater. Interfaces*. 4 (22) (2017) 1700629. <https://doi.org/10.1002/admi.201700629>.
- [70] E.B. Joyee, Y. Pan, A fully three-dimensional printed inchworm-inspired soft robot with magnetic actuation, *Soft Robot*. 6(3) (2019) 333-345.  
<https://doi.org/10.1089/soro.2018.0082>.
- [71] Lu, P. Guo, Y. Pan, Magnetic-Field-Assisted Projection Stereolithography for Three-Dimensional Printing of Smart Structures, *J. Manuf. Sci. Eng. Trans. ASME*. 139(7) (2017) 071008. <https://doi.org/10.1115/1.4035964>.

- [72] G. Shao, H.O.T. Ware, J. Huang, R. Hai, L. Li, C. Sun, 3D printed magnetically-actuating micro-gripper operates in air and water, *Addit. Manuf.* 38 (2021) 101834. <https://doi.org/10.1016/j.addma.2020.101834>.
- [73] B. Nagarajan, P. Mertiny, A.J. Qureshi, Magnetically loaded polymer composites using stereolithography—Material processing and characterization, *Mater. Today Commun.* 25 (2020) 101520. <https://doi.org/10.1016/j.mtcomm.2020.101520>.
- [74] W. Hu, G.Z. Lum, M. Mastrangeli, M. Sitti, Small-scale soft-bodied robot with multimodal locomotion, *Nature.* 554 (2018) 81-85. <https://doi.org/10.1038/nature25443>.
- [75] H. Lu, M. Zhang, Y. Yang, Q. Huang, T. Fukuda, Z. Wang, Y. Shen, A bioinspired multilegged soft millirobot that functions in both dry and wet conditions, *Nat. Commun.* 9 (2018) 3944. <https://doi.org/10.1038/s41467-018-06491-9>.
- [76] Y. Kim, H. Yuk, R. Zhao, S.A. Chester, X. Zhao, Printing ferromagnetic domains for untethered fast-transforming soft materials, *Nature.* 554 (2018) 81-85. <https://doi.org/10.1038/s41586-018-0185-0>.
- [77] H. Ceylan, I.C. Yasa, O. Yasa, A.F. Tabak, J. Giltinan, M. Sitti, 3D-Printed Biodegradable Microswimmer for Theranostic Cargo Delivery and Release, *ACS Nano.* 13(3) (2019) 3353-3362. <https://doi.org/10.1021/acsnano.8b09233>.
- [78] C. Peters, O. Ergeneman, P.D.W. García, M. Müller, S. Pané, B.J. Nelson, C. Hierold, Superparamagnetic twist-type actuators with shape-independent magnetic properties and surface functionalization for advanced biomedical applications, *Adv. Funct. Mater.* 24(33) (2014) 5296-5276. <https://doi.org/10.1002/adfm.201400596>.
- [79] J.J. Martin, B.E. Fiore, R.M. Erb, Designing bioinspired composite reinforcement architectures via 3D magnetic printing, *Nat. Commun.* 6 (2015) 8641. <https://doi.org/10.1038/ncomms9641>.
- [80] H. Wang, Y. Yu, Y. Sun, Q. Chen, Magnetic nanochains: A review, *Nano.* 6(1) (2011) 1-17. <https://doi.org/10.1142/S1793292011002305>.
- [81] K. Thorkelsson, P. Bai, T. Xu, Self-assembly and applications of anisotropic nanomaterials: A review, *Nano Today.* 10(1) (2015) 48-66. <https://doi.org/10.1016/j.nantod.2014.12.005>.
- [82] G. Palmara, F. Frascella, I. Roppolo, A. Chiappone, A. Chiadò, Functional 3D printing: Approaches and bioapplications, *Biosens. Bioelectron.* 175 (2021) 112849, <https://doi.org/10.1016/j.bios.2020.112849>.
- [83] L.Y. Zhou, J. Fu, Y. He, A Review of 3D Printing Technologies for Soft Polymer

- Materials, *Adv. Funct. Mater.* 30(28) (2020) 2000187,  
<https://doi.org/10.1002/adfm.202000187>
- [84] S. Lantean, G. Barrera, C.F. Pirri, P. Tiberto, M. Sangermano, I. Roppolo, G. Rizza, 3D Printing of Magnetoresponse Polymer Materials with Tunable Mechanical and Magnetic Properties by Digital Light Processing, *Adv. Mater. Technol.* 4(11) (2019) 190505. <https://doi.org/10.1002/admt.201900505>.
- [85] C.H. Bennett, Exact Defect Calculations in Model Substances, in: *Diffus. Solids*, 1975, 73-113. <https://doi.org/10.1016/b978-0-12-522660-8.50007-6>.
- [86] J.R. Beeler, Jr, R.E. Dahl, Jr, R.D. Bourquin, Structure, Energy and Atom Migration Effects of Tilt Boundaries, *Le J. Phys. Colloq.* (1975).  
<https://doi.org/10.1051/jphyscol:1975411>.
- [87] A. Darras, E. Opsomer, N. Vandewalle, G. Lumay, Superparamagnetic colloids in viscous fluids, *Sci. Rep.* 7 (2017) 7778. <https://doi.org/10.1038/s41598-017-07917-y>.
- [88] L. Ratke, P.W. Voorhees, Growth and coarsening: Ostwald ripening in materials processing, *Choice Rev. Online.* (2002). <https://doi.org/10.5860/choice.39-6445>.
- [89] D. Mostarac, E. V. Novak, P.A. Sánchez, S.S. Kantorovich, The impact of magnetic field on the conformations of supracolloidal polymer-like structures with superparamagnetic monomers, *J. Mol. Liq.* 305 (2020) 112761.  
<https://doi.org/10.1016/j.molliq.2020.112761>.
- [90] D. Mostarac, P.A. Sánchez, S. Kantorovich, Characterisation of the magnetic response of nanoscale magnetic filaments in applied fields, *Nanoscale.* 12 (2020) 13933-13947.  
<https://doi.org/10.1039/d0nr01646b>.
- [91] A.A. Kuznetsov, Equilibrium properties of magnetic filament suspensions, *J. Magn. Magn. Mater.* 470 (2019) 28-32. <https://doi.org/10.1016/j.jmmm.2017.10.091>.
- [92] W. Zhang, P.K.J. Wong, D. Zhang, J. Yue, Z. Kou, G. van der Laan, A. Scholl, J.G. Zheng, Z. Lu, Y. Zhai, XMCD and XMCD-PEEM Studies on Magnetic-Field-Assisted Self-Assembled 1D Nanochains of Spherical Ferrite Particles, *Adv. Funct. Mater.* 27(29) (2017) 1701265. <https://doi.org/10.1002/adfm.201701265>.
- [93] Y. Zhang, L. Sun, Y. Fu, Z.C. Huang, X.J. Bai, Y. Zhai, J. Du, H.R. Zhai, The shape anisotropy in the magnetic field-assisted self-assembly chain-like structure of magnetite, *J. Phys. Chem. C.* 113(19) (2009) 8152-8157.  
<https://doi.org/10.1021/jp807937d>.
- [94] I.S. Novikau, P.A. Sánchez, S.S. Kantorovich, The influence of an applied magnetic field on the self-assembly of magnetic nanogels, *J. Mol. Liq.* 307 (2020) 112902.



<https://doi.org/10.1016/j.molliq.2020.112902>.

- [95] Y. Men, W. Wang, P. Xiao, J. Gu, A. Sun, Y. Huang, J. Zhang, T. Chen, Controlled evaporative self-assembly of Fe<sub>3</sub>O<sub>4</sub> nanoparticles assisted by an external magnetic field, *RSC Adv.* 5 (2015) 31519-31524. <https://doi.org/10.1039/c5ra02160j>.
- [96] B.M. Smirnov, E.E. Son, D. V Tereshonok, Diffusion and mobility of atomic particles in a liquid, *J. Exp. Theor. Phys.* 125 (2017) 906–912. <https://doi.org/https://doi.org/10.1134/S1063776117110073>.
- [97] M.A.M. Gijs, Magnetic bead handling on-chip: New opportunities for analytical applications, *Microfluid. Nanofluidics.* 1(2004) 22-40. <https://doi.org/10.1007/s10404-004-0010-y>.
- [98] N. Pamme, Magnetism and microfluidics, *Lab Chip.* 6 (2006) 24-38. <https://doi.org/10.1039/b513005k>.
- [99] S. Melle, J.E. Martin, Chain model of a magnetorheological suspension in a rotating field, *J. Chem. Phys.* 118(21) (2003) 9875-9881. <https://doi.org/10.1063/1.1570817>.
- [100] S. Melle, O.G. Calderón, M.A. Rubio, G.G. Fuller, Rotational dynamics in dipolar colloidal suspensions: Video microscopy experiments and simulations results, *J. Nonnewton. Fluid Mech.* 102(2) (2002) 135-148. [https://doi.org/10.1016/S0377-0257\(01\)00174-4](https://doi.org/10.1016/S0377-0257(01)00174-4).
- [101] A.K. Vuppu, A.A. Garcia, M.A. Hayes, Video Microscopy of Dynamically Aggregated Paramagnetic Particle Chains in an Applied Rotating Magnetic Field, *Langmuir.* 19(21) (2003) 8646-8653. <https://doi.org/10.1021/la034195a>.
- [102] S. Melle, O.G. Calderón, M.A. Rubio, G.G. Fuller, Microstructure evolution in magnetorheological suspensions governed by Mason number, *Phys. Rev. E - Stat. Physics, Plasmas, Fluids, Relat. Interdiscip. Top.* 68(4) (2003) 041503. <https://doi.org/10.1103/PhysRevE.68.041503>.

# Supporting Information

## Programming the microstructure of magnetic nanocomposites in DLP 3D printing

Simone Lantean<sup>1,2</sup>, Ignazio Roppolo<sup>1,3\*</sup>, Marco Sangermano<sup>1</sup>, Marc Hayoun<sup>2</sup>, Hichem Dammak<sup>2,4</sup>, Giancarlo Rizza<sup>2</sup>

1. Department of Applied Science and Technology, Politecnico di Torino, Duca degli Abruzzi, 24, 10124, Torino, Italy
2. Laboratoire des Solides Irradiés (LSI), Institut Polytechnique de Paris, CEA/DRF/IRAMIS, CNRS, Ecole polytechnique, Route de Saclay, 91128 Palaiseau, France
3. Center for Sustainable Future Technologies, Istituto Italiano di Tecnologia, Via Livorno 60, 10144, Torino, Italy
4. Laboratoire Structures Propriétés et Modélisation des Solides, CentraleSupélec, CNRS, Université Paris-Saclay, F 91190 Gif-sur-Yvette, France

E-mail: ignazio.roppolo@polito.it

## Table of contents

1. Modeling and simulation method
2. Application of the magnetic field during optical microscopy observations
3. Image Analysis
4. Optical microscopy
  - 4.1 Additional results on the self-assembly process
  - 4.2 Additional results on the rotation of the magnetic chains
5. 3D Printer modification

### 1. Modeling and simulation method

The aim is the simulation of the generic behavior of the system in response to an external magnetic field and its rotation. Hence, the modeling of the Fe<sub>3</sub>O<sub>4</sub> NPs by superparamagnetic NPs and the absence of the fluid.

In this case their susceptibility  $\chi \gg 1$ , and the induced magnetization,  $\mathbf{m}_j$ , of each  $j^{th}$  NP is parallel to the local induction,  $\mathbf{B}_j$ :

$$\mathbf{m}_j = \frac{\pi d^3}{6\mu_0} \mathbf{B}_j \quad (\text{eq. S1})$$

where  $d$  is the NP diameter and  $\mu_0$  the vacuum permeability.  $\mathbf{B}_j$  results from the external and internal contributions:

$$\mathbf{B}_j = \mathbf{B}_{ext} + \sum_{i \neq j} \mathbf{B}(\mathbf{m}_i, \mathbf{r}_{ij}) \quad (\text{eq. S2})$$

where  $\mathbf{r}_{ij}$  is the vector of the two-particle chain axis, and  $\mathbf{B}(\mathbf{m}_i, \mathbf{r}_{ij})$  the magnetic induction created by the magnetization  $\mathbf{m}_i$  on the  $j^{th}$  NP obtained in the dipolar approximation:

$$\mathbf{B}(\mathbf{m}_i, \mathbf{r}_{ij}) = \frac{\mu_0}{4\pi} \frac{3(\mathbf{m}_i \cdot \mathbf{u}_{ij}) \mathbf{u}_{ij} - \mathbf{m}_i}{r_{ij}^3} \quad (\text{eq. S3})$$

with  $\mathbf{u}_{ij}$  is the unit vector.

The total potential energy is given by:

$$U = - \sum_j \mathbf{m}_j \cdot \mathbf{B}_j + \sum_j \sum_{i < j} \frac{A}{r_{ij}^{12}} \quad (\text{eq. S4})$$

The first term is attractive and the second one is the usual repulsive Lennard-Jones contribution to prevent overlapping between NPs.

All quantities have been reduced as follows: distance by  $d$ , magnetization by  $\frac{4\pi d^3}{\mu_0} \mathbf{B}_{ext}$ , energy by  $\frac{4\pi d^3}{\mu_0} B_{ext}^2$ , time by  $\sqrt{\frac{\mu_0 M}{4\pi d B_{ext}^2}}$  where  $M$  is the NP mass, and magnetic induction by  $\mathbf{B}_{ext}$ . The reduced value of the constant  $A$  (0.2083) was chosen to lead to an equilibrium separate distance between NPs of about  $1.2 d$ .

A system of 1000 (thousand) NPs in a cubic box of  $43.5 \times 43.5 \times 43.5 d^3$  was chosen to reproduce the experimental NPs volume fraction of 3 wt.% ( $6.1 \cdot 10^{-3}$ ) and periodic boundary conditions were applied.

In a second set of simulations, the magnetic direction was rotated around the  $z$  axis by an angle of  $\theta_B$  from the  $x$  axis, and the relaxation of the NP positions was carried out for eight values, i. e.  $5^\circ$ ,  $10^\circ$ ,  $15^\circ$ ,  $30^\circ$ ,  $40^\circ$ ,  $45^\circ$ ,  $50^\circ$  and  $60^\circ$ . The evolution of the mean rotation angle,  $\theta$ , of the NP chains is given in Figures 7.c and 7.d. The angular distribution of NP chains has been studied. The evolution of the standard deviation  $\sigma_\theta$  is given in Figure S1. The width of the angular distribution increases with time, reaches a maximum value at  $t_{max}^*$ , and then decreases. This behavior depends on  $\theta_B$  and confirms the existence of the two ranges of angles already mentioned as clearly pointed out by the inset of Figure S1.

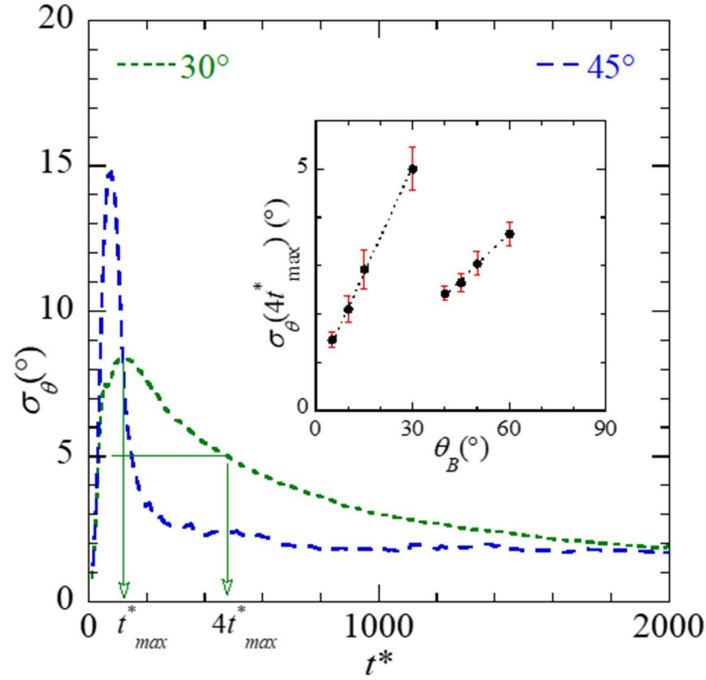


**Figure S1:** Evolution of the standard deviation,  $\sigma_\theta$ , of the rotation angle of the NP chains as a function of the reduced time during the relaxation to the equilibrium state. The maximum values of  $\sigma_\theta$  are obtained at  $t_{max}^*$ , which depends on  $\theta_B$ . The green arrows refer to the case  $\theta_B = 30^\circ$ . The inset shows the values of  $\sigma_\theta$  selected at  $4t_{max}^*$  as a function of  $\theta_B$ . Dashed lines are guides for the eye.

## 2. Application of the magnetic field during optical microscopy observations

Figure S2 shows the customized 3D printed experimental device we used to apply a static magnetic field and, at the same time, to observe the self-assembly process by optical microscopy. The support consists of several parts to be assembled, allowing a discrete displacement of the NdBF<sub>e</sub> magnets (Figure S2 a,b). The empty space in the central unit, i.e. 1x1 cm<sup>2</sup>, it is used as optical window for observations with the microscope. Here, it is placed a glass slide on which a drop of the formulation (a circle of approximately 1cm of diameter) containing the magnetic NPs is deposited. Changing the distance between the magnets,  $d$ , it is possible to control the intensity of the applied magnetic field (Figure S2 c). The field gradient measured in the area of the sample corresponds to 0.5 mT/cm for the 6 mT field, and 3 mT/cm for the 30 mT field. No NPs migration towards the magnets was observed for both configurations. All the parts were 3D printed with RobotFactory RED resin by the RobotFactory HD 2.0 DLP printer.

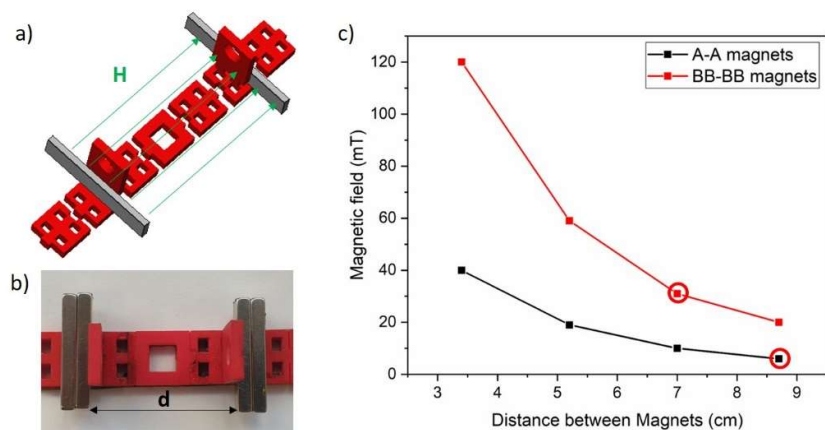


**Figure S2:** a) Sketch of the 3D printed support to control the spacing between a couple of permanent magnets. b) The 3D printed support. C) The magnetic field intensity measured by varying the distance between A-A and BB-BB set of magnets.

### 3. Image Analysis Method

To perform Image analysis, first the full-colors images collected by optical microscopy were converted into grey-scales pictures, and finally the contrast and brightness were adjusted to achieve black and white images of the microstructures. For a correct evaluation of the dimensions of the aggregates, the contrast and brightness parameters were maintained constant for all the pictures taken in a single experimental series. Particle analysis was performed by ImageJ approximating the aggregates to ellipses, and measuring their width, length and angle. To improve the quality of the results, the aggregates placed at the edges of the pictures were not considered.

As the images correction leads to artifacts such as isolated pixel, the results were filtered to aggregates longer than 4 pixels.

The data concerning the angle of the chains were manipulated to transform the angles larger than  $90^\circ$  into negative angles and facilitate the analysis of the results.

The error bars on the average values were calculated as the product of the standard deviation ( $\sigma_s$ ) and the square root of the reciprocal of the number of the measured aggregates ( $N$ ):

$$\sigma_m = \frac{\sigma_s}{\sqrt{N}}$$

## 4. Optical microscopy observations

### 4.1 Additional results on the self-assembly process

In Figure S3 are reported the optical images of the 60Eb40BA\_3NPs sample exposed to an external field of 30mT.

In Figure S4 are reported the optical images taken characterizing the self-assembly process of three different samples: 60Eb40BA\_3NPs\_6mT, 67Eb33BA\_3NPs\_30mT, 60Eb40BA\_0.5NPs\_30mT

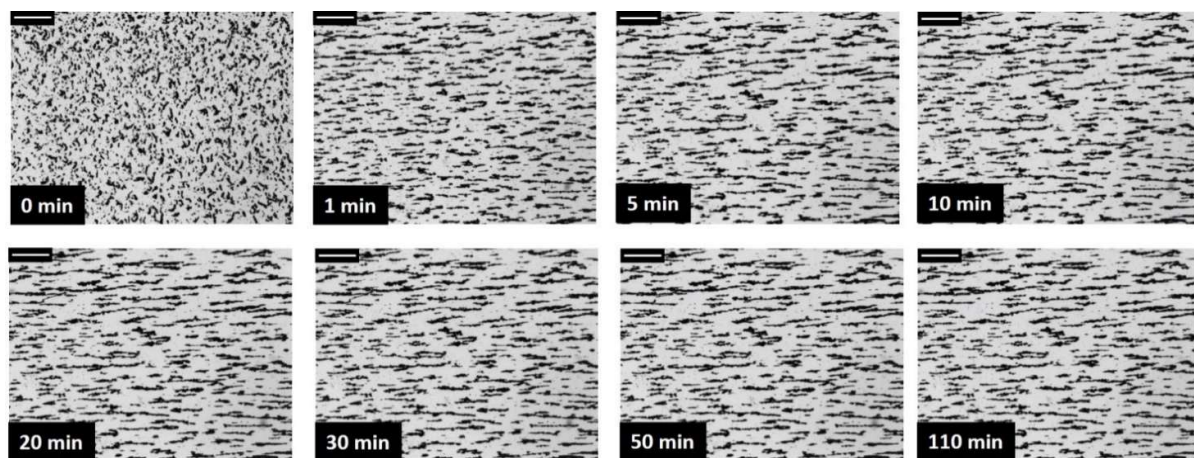


**Figure S3:** Evolution of the microstructure of 60Eb40BA\_3NPs\_30mT sample used as reference. Scale bar is 500  $\mu\text{m}$ .

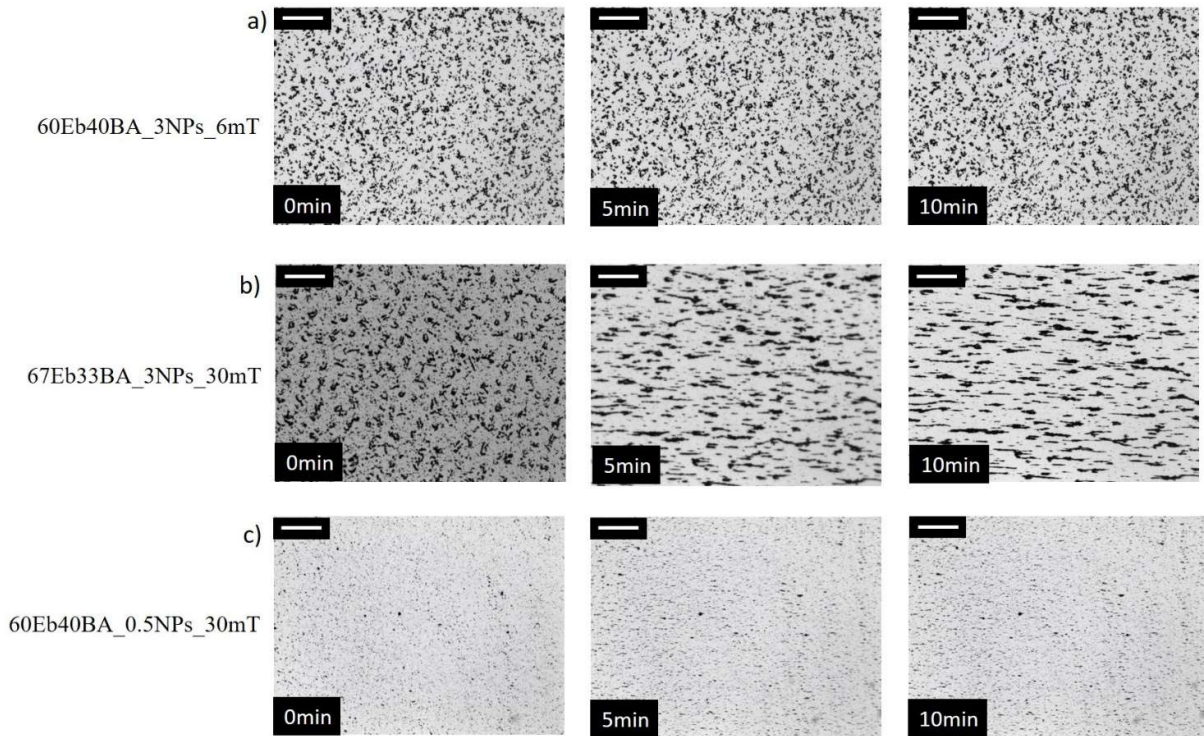


**Figure S4:** Evolution of the microstructure of a) 60Eb40BA\_3NPs\_6mT, b) 67Eb33BA\_3NPs\_30mT, and c) 60Eb40BA\_0.5NPs\_30mT. Scale bar is 500  $\mu\text{m}$ .

## 4.2 Additional results on the rotation of the magnetic chains

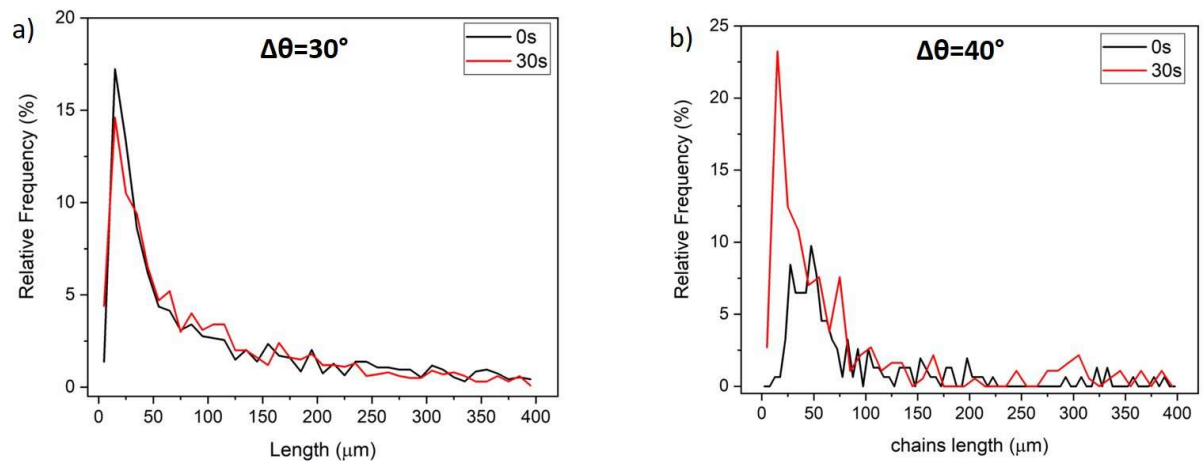


**Figure S5:** Evolution of the distribution of the length of the magnetic chains for an external field rotation of a)  $30^\circ$ , and b)  $40^\circ$ .

The influence of the viscosity on the rotation of the magnetic chains was evaluated. For this purpose, it was prepared a formulation with consistent higher viscosity, namely 85Eb15BA\_3NPs formulation ( $\eta = 0.580 \text{ Pa s}$ ), and the results were compared with the

standard formulation 60Eb40BA\_3NPs ( $\eta = 0.048$  Pa s). In this case, two magnetic field angles were tested:  $10^\circ$  and  $30^\circ$ . Even though the viscosity values of the two formulations differed by one order of magnitude, the rotation kinetics were similar for both the tested  $\Delta\theta_B$ , except for a small delay in the kinetics for the more viscous formulation, i.e. 85Eb15BA\_3NPs (Figure S6). This suggests that the rotation process is not strongly influenced by the medium viscosity.

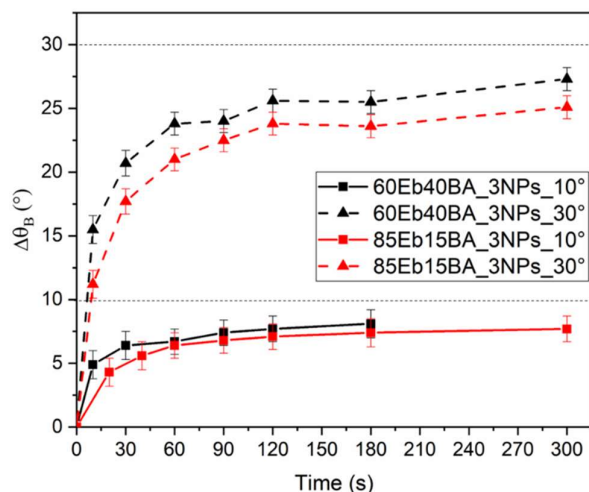


**Figure S6** :Comparison of the rotation kinetics between the 75Eb15BA\_3NPs and 60Eb40BA\_3NPs formulations for  $\Delta\theta_B = 10^\circ$ , and  $30^\circ$ .

## 5. 3D Printer modification

The developed solution to produce controlled magnetic fields during the 3D printing process consists in using a couple of permanent magnets stuck on a rotating ball bearing. The ball bearing, purchased from SKF ([www.skf.com](http://www.skf.com)), is 10 mm thick with an external diameter of 70 mm, whereas the diameter of the central hole is 40 mm. To avoid perturbation of the applied magnetic field, all the ball-bearing components are non-magnetic materials, i.e. the whole cage is made of nylon, whereas the rotating balls of glass.

The addition of the ball-bearing in the printing plane led to some modifications to the original set-up of the HD 2.0+ RobotFactory. First, the original metallic vat of the printer has been removed and the ball bearing were fixed onto the bottom glass of the vat. In the HD 2.0+ RobotFactory, this glass plate is covered with a protective film (named *siligel*) which is fixed to the metallic vat through a screws system. The *siligel* is compulsory for the printing process as it ensures the detachment of the printed layers from the printing area. To maintain the *siligel* anchored to the printing glass, a PLA structure with the same dimensions of the original vat and reproducing the exact screw-holes was 3D printed using FFF 3D printer (FlashForge Creator



Pro). As it is not possible to accurately reproduce the threading of the holes, the PLA structure was fixed to the glass with a system of aluminum screws and nuts. Thanks to this solution the inner hole of the ball bearing became the new resins reservoir where the photocurable formulation can be poured. Finally, as the addition of ball bearing as a new resin reservoir limits the printing area to the dimension of the hole, a custom glass cylinder with a diameter of 25 mm and a height of 40 mm was crafted and glued to the platform acting as build platform. It is worth mentioning that using this configuration, the added elements neither interfere with the projected light nor deflect the magnetic field produced by the magnets. In Figure S7 is reported a sketch of the proposed printer set-up, as well as, the modification elements.

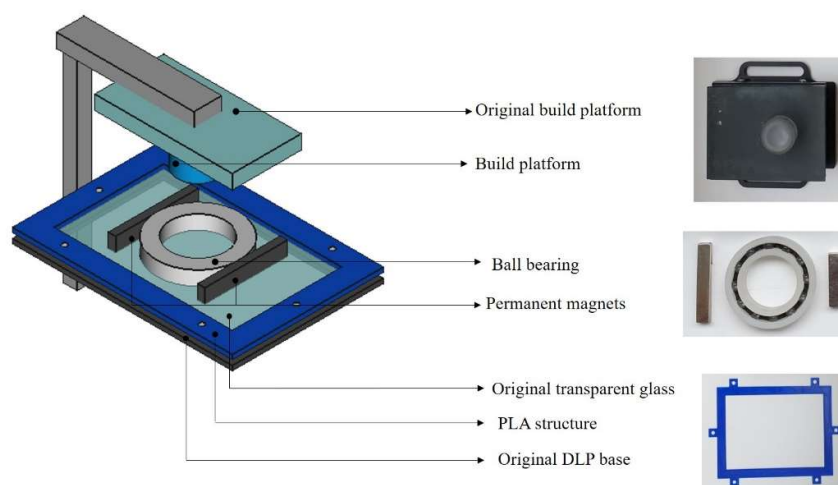


**Figure S7:** Sketch of the proposed magneto-assisted DLP printer set-up.

### **Experimental set-up to control the rotation of the chains**

A linear-to-rotary actuator controlled by an Arduino microcontroller was design to regulate the rotation of the external wall of the ball bearing, i.e. the applied field vector. The device consists of three main parts: i) a drive wheel linked to a servomotor controlled by an Arduino microcontroller (Figure S8a), ii) a double-sided rack (Figure S8b) which allows to transform the rotation of the drive wheel into translation, and connected by seven pillars to transfer the translation to a iii) drilled sprocket (Figure S8c) fixed on the external wall of the ball bearing. Therefore, the rotation of the drive wheel is transferred to the back and forward motion of the rack, and the latter allows the ball bearing to rotate (Figure S8d). In video S1 the set-up is show in operation.

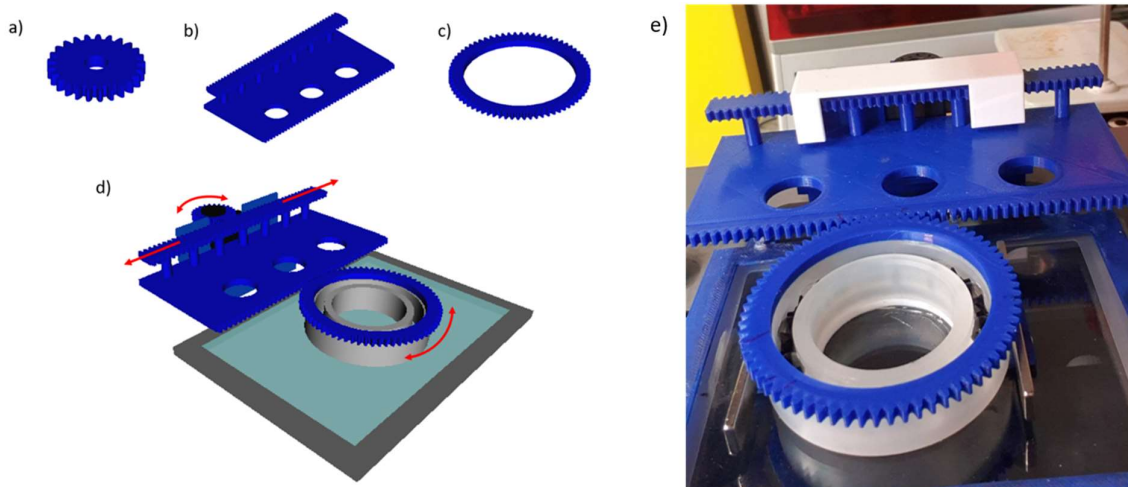


**Figure S8:** Components of the linear to rotatory soft actuator used to tilt the magnetic field: a) STL file of the drive wheel connected to the servomotor, b) STL file of the rack, and c) STL file of the drilled sprocket fixed on the ball bearing. d) STL files of the set-up and e) final actuator set-up in a DLP printer.

## References

- [1] J. R. Beeler, Jr., G. L. Kulcinski, dans *Interatomic potentials and simulation of lattice defects*, P. C. Gehlen, J. R. Beeler, Jr., R. I. Jaffee, eds, 735 (Plenum Press, New York, 1972).  
Agenda discussion: computer techniques.
- [2] C. H. Bennett, dans *Diffusion in solids: Recent developments*, A. S. Nowick, J. J. Burton, eds, 73 (Academic Press, New York, 1975). Exact defect calculations in model substances.